Journal of Materials Science & Technology 223 (2025) 76–90

Contents lists available at ScienceDirect

Journal of Materials Science & Technology

journal homepage: www.elsevier.com/locate/jmst

Research Article

Prussian blue analogue-derived porous nanocages with hollow (Co,Fe)O nanoparticles as anodes for lithium ion batteries

Jae Seob Lee[a,b,1], Kun Woo Baek[a,1], Narasimharao Kitchamsetti[a], Hyun Woo Kim[c], Jung Sang Cho[a,d,e,*]

[a] Department of Engineering Chemistry, Chungbuk National University, Chungbuk 28644, Republic of Korea
[b] Department of Materials Science and Engineering, Korea University, Anam-Dong, Seongbuk-Gu, Seoul 02841, Republic of Korea
[c] Korea Basic Science Institute, 169-148 Gwahak-ro Yuseong-gu, Daejeon 34133, Republic of Korea
[d] Biomedical Research Institute, Chungbuk National University Hospital, Chungbuk 28644, Republic of Korea
[e] Advanced Energy Research Institute, Chungbuk National University, Cheongju, Chungbuk 28644, Republic of Korea

ARTICLE INFO

Article history:
Received 26 July 2024
Revised 7 October 2024
Accepted 12 October 2024
Available online 16 November 2024

Keywords:
CoFe-Prussian blue analogue
Polydopamine-derived carbon
Porous nanocages
Hollow (Co,Fe)O nanoparticles
Kirkendall diffusion mechanism
Lithium-ion batteries

ABSTRACT

CoFe-Prussian blue analog (CoFe-PBA) template derived porous nanocages comprising hollow (Co,Fe)O nanoparticles are introduced as a highly efficient anode for lithium-ion batteries (LIBs) by integrating the co-precipitation and nanoscale Kirkendall diffusion processes. This strategic approach employs a solution-based facile polydopamine (PDA)-derived carbon coating process to control the oxidation rate of nanoparticles during subsequent heat treatment to achieve the hollow structure by the nanoscale Kirkendall diffusion effect. The application of different concentrations of PDA to the nanocages resulted in the formation of porous nanocages of three types, such as (Co,Fe)O@PDA-C-20, (Co,Fe)O@PDA-C-100, and (Co,Fe)O@PDA-C-200. Notably, (Co,Fe)O@PDA-C-100 porous nanocages exhibit remarkable cycling stability by the hollow structured (Co,Fe)O nanoparticles. Additionally, the hollow and porous structures facilitate rapid charge species diffusion, efficient electrolyte infiltration, and effective management of volumetric changes. When used as anodes for LIBs, the hollow (Co,Fe)O@PDA-C-100 anodes demonstrate impressive structural robustness and high-rate performance. They exhibit remarkable structural integrity, demonstrating stable cycling performance for up to 300 cycles at 0.5 and 1.0 A g^{-1} (capacity retentions of 99.3% and 97.2%, respectively). In terms of rate capability, the hollow (Co,Fe)O@PDA-C-100 porous nanocages exhibit a high discharge capacity of 284 mA h g^{-1} at 10 A g^{-1}. Moreover, the practical application potential of the prepared hollow (Co,Fe)O@PDA-C-100 anode is demonstrated by a full-cell test paired with and $Li(Ni_{0.8}Co_{0.1}Mn_{0.1})O_2$ cathode under the condition of practical application. This clearly highlights the structural advantages of the prepared hollow (Co,Fe)O@PDA-C-100 porous nanocages.

1. Introduction

Scientists have a keen interest in hollow metal oxide composite nanostructures that have controlled internal voids and shell thicknesses. These structures possess intriguing chemical and physical properties, making them valuable for various applications, such as catalysis, drug delivery, and energy storage [1,2]. In recent times, multiple techniques have emerged for the fabrication of these structures, including the utilization of nanoscale Kirkendall diffusion effect [3,4], chemical etching [5,6], and template-assisted methods [7–9]. Compared to other methods, the nanoscale Kirkendall diffusion effect allows for the fabrication of hollow metal oxide composite nanostructures that are smaller in size and have more uniform shapes. For example, using this technique, hollow α-Fe_2O_3 and Fe_3O_4 nanoparticles with diameters less than 15 nm and shell thicknesses of around 4 nm were prepared [10,11]. These smaller and more uniform hollow metal oxide composites can be used as ideal building blocks for lightweight structural composites. However, up until now, these hollow composite nanostructures have only been produced in solvent systems that contain toxic organic components such as oleyl amine, octadecene, and trimethylamine N-oxide [12,13]. Therefore, it is highly desirable to develop a simple and practical strategy for the production of well-defined hollow composite nanostructures.

* Corresponding author at: Department of Engineering Chemistry, Chungbuk National University, Chungbuk 28644, Republic of Korea.
E-mail address: jscho@cbnu.ac.kr (J.S. Cho).
[1] These authors contributed equally to this work.

https://doi.org/10.1016/j.jmst.2024.10.026
1005-0302/

Rechargeable Li-ion batteries (LIBs) are crucial for portable electronic devices, hybrid electric vehicles, and aerospace technology. Transition metal (Co,Fe) oxide composites show great potential as high-energy-density materials due to their high theoretical capacity (1000 mA h g^{-1}), non-toxic nature, and low cost [14,15]. However, their use as an electrode for high-energy-density LIBs has been hindered by their low electrical conductivity, significant volumetric changes during cycling, and the intrinsic kinetic limitations of (Co,Fe) oxides. To address these issues and improve the structural integrity and electrical conductivity of (Co,Fe) oxides, several strategies have been developed: 1) decreasing the particle size of (Co,Fe) oxides to enable fast transport of electrons and ions [9,16,17]; 2) fabricating hollow (Co,Fe) oxides to accommodate volume changes during cycling [18,19]; 3) dispersing (Co,Fe) oxides in a porous structure to facilitate the electrolyte penetration into the nanostructure [20,21]. These strategies have significantly enhanced the electrochemical performance of (Co,Fe) oxides. However, the long-term cycling stability of anodes based on transition metal oxides, especially at higher current densities, remains unsatisfactory.

CoFe-Prussian blue analogues (PBAs) are a significant type of crystalline inorganic-organic hybrids. They are coordinated to rigid organic molecules and can serve as a unique precursor for creating porous hollow composite nanostructures ranging from 0- to 3-dimensions [2]. In this particular study, we utilized a co-precipitation technique to prepare nanocages made of CoFe-PBAs. We then coated these nanocages with polydopamine (PDA) to form Prussian blue analogue derived porous nanocages comprising hollow (Co,Fe)O nanoparticles (denoted as (Co,Fe)O@PDA-C porous nanocages), utilizing the nanoscale Kirkendall diffusion effect. The PDA layer coated on the nanocage inhibits the infinite crystal growth and aggregation of the CoFe nanoparticles during subsequent carbonization heat treatment. Moreover, the PDA-derived carbon transfers thermal energy to the CoFe nanocrystals by combusting to CO_2 during the oxidation process, affecting the oxidation rate of the metallic species by modulating their thermal behavior. This plays a key role in the formation of hollow (Co,Fe)O nanoparticles through the nanoscale Kirkendall diffusion effect. Compared to existing methods for creating hollow composites of transition metal oxides, our synthesis of hollow (Co,Fe)O@PDA-C porous nanocages offers several advantages. Firstly, this process does not use any toxic organic components such as string acid, making it environmentally friendly and easily scalable for industrial applications. Additionally, this approach facilitates the formation of hollow (Co,Fe)O nanoparticles through the nanoscale Kirkendall diffusion effect by utilizing a simple solution-based coating method, in contrast to conventional heat treatment processes that require sensitive and complex control of parameters such as temperature, time, and heating rate. Finally, incorporating empty space into the hollow (Co,Fe)O@PDA-C nanocage addresses the issue of volumetric expansion, and the anchoring of the hollow (Co,Fe)O nanoparticles within the PBA-derived porous scaffolds significantly prevents their aggregation. This enhancement contributes to the long-term cycling stability of the composite anode, especially at higher current densities. Consequently, the synthesized hollow (Co,Fe)O@PDA-C composites demonstrate outstanding electrochemical performances that surpass those of most previously reported transition metal oxide nanostructures.

2. Experimental

2.1. Preparation of CoFe-PBA nanocages

In a standard synthesis method, 0.30 g of cobalt (II) acetate tetrahydrate (from Sigma Aldrich, purity: 98%, M.W: 249.08) and 0.441 g of trisodium citrate dihydrate (from Sigma Aldrich, purity: 99%, M.W: 294.10) were dissolved in 60 mL of deionized (DI) water, forming solution A. Simultaneously, 0.264 g of potassium hexacyanoferrate (III) (from Sigma Aldrich, purity: 99%, M.W: 329.24) were dissolved in another 60 mL of DI water to create solution B. Subsequently, solution B was slowly added to solution A while employing magnetic stirring. Following 5 min of continuous stirring, the resulting mixed solution was left to age at room temperature for 24 h. The resulting precipitate was gathered via centrifugation, washed sequentially with DI water and ethanol, and then dried at 70 °C overnight.

2.2. Preparation of (Co,Fe)O@PDA-C nanocages

The as-prepared CoFe-PBA nanocages (0.1 g) were dispersed in 100 mL of tris buffer solution (0.01 mol/L, pH: 8.7) to prepare the PDA-coated CoFe-PBA (denoted as CoFe-PBA@PDA) nanocages. Subsequently, three different concentrations of dopamine hydrochloride (Sigma Aldrich, 98%, M.W: 189.64), specifically 20, 100, and 200 mg, were separately added to the solution and stirred for 24 h under ambient conditions. Afterward, the CoFe-PBA@PDA nanocages underwent multiple washes with DI water, were collected via centrifugation, and then dried in an oven at 60°C. Following this, the CoFe-PBA@PDA nanocages obtained after drying were placed in a crucible. The carbonization process was carried out for 3 h at 400 °C under N_2 atmosphere and subsequently held at 400 °C for 3 h in an air environment, to produce the (Co,Fe)O@PDA-C nanocages, denoted as (Co,Fe)O@PDA-C-20, (Co,Fe)O@PDA-C-100, and (Co,Fe)O@PDA-C-200 porous nanocages for the respective dopamine hydrochloride concentrations. For comparison, a sample without PDA coating, referred to as (Co,Fe)O nanocages was also prepared. In brief, the CoFe-PBA nanocages obtained after drying were subjected to carbonization followed by oxidation under the same identical conditions to obtain the (Co,Fe)O nanocages.

2.3. Preparation of bare (Co,Fe)O nanocrystals

Bare (Co,Fe)O nanocrystals were also prepared for comparison. To do so, 0.03 mmol/L of cobalt (II) acetate tetrahydrate (Sigma Aldrich, 98%, M.W: 249.08) and 0.01 mmol/L of iron chloride (III) hexahydrate (Sigma Aldrich, 99%, M.W: 270.30) were thoroughly ground using a mortar and pestle. The resulting powder was transferred to a crucible and subjected to carbonization followed by oxidation under the same identical conditions to achieve the (Co,Fe)O nanocrystals.

2.4. Electrochemical measurements

2032-type coin cells were assembled in an Ar-filled glove box at room temperature (26 °C) to evaluate the performance of the composite porous nanocages in LIBs. The working electrodes were prepared using a slurry casting method by homogeneously dispersing the active material, conductive carbon (Super-P), and sodium carboxymethyl cellulose as a binder in distilled water at a weight ratio of 7:2:1. They were then deposited onto Cu substrates and dried overnight at 60 °C in a hot air oven. Lithium metal served as both the reference and counter electrode. Circular electrodes (ϕ = 14 mm) with an average active material mass loading of ~1 mg cm^{-2} were prepared and transferred into the glove box. Microporous polypropylene films (Celgard® 2400) were used as separators. The electrolyte, consisting of 1 mol/L $LiPF_6$ dissolved in a mixture of fluoroethylene carbonate and dimethyl carbonate with a 1:1 volume ratio, was prepared. To evaluate the full-cell performance, the cathodes were prepared by casting a slurry of $Li(Ni_{0.8}Co_{0.1}Mn_{0.1})O_2$ (NCM811) powder, Super-P, and poly(vinylidene fluoride) at a weight ratio of 8:1:1 in 1-methyl-2-pyrrolidinone (NMP) solvent onto an Al current collector. The

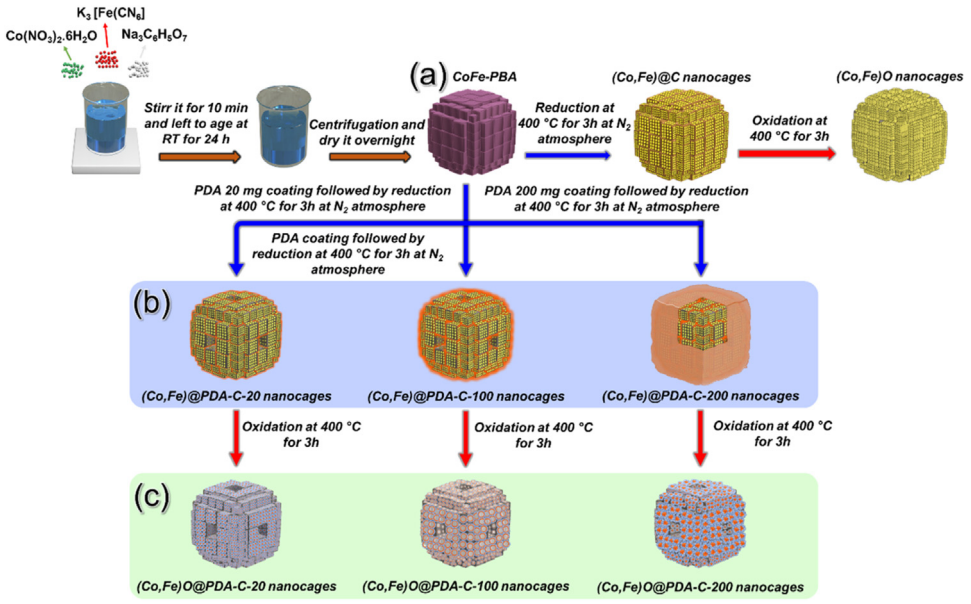

Scheme 1. Pictorial illustration for synthesizing (Co,Fe)O, (Co,Fe)O@PDA-C-20, (Co,Fe)O@PDA-C-100, and (Co,Fe)O@PDA-C-200 porous nanocages using co-precipitation technique followed by Kirkendall-type diffusion.

electrochemical performance of anodes was assessed using cyclic voltammetry (CV), charge-discharge, electrochemical impedance spectroscopy (EIS), and galvanostatic intermittent titration technique (GITT) analysis. CV analysis was conducted at a scan rate of 0.1 mV s^{-1}. Charge-discharge tests were performed at various current densities ranging from 0.1 A g^{-1} to 10.0 A g^{-1} using a WBCS3000 (WonATech) cycler. The voltage window for all electrochemical tests was set at 0.001–3.0 V. EIS (ZIVE SP1) measurements were carried out in the frequency range of 0.01–100 kHz using a signal amplitude of 10 mV. GITT analysis was performed at a constant current density of 0.1 A g^{-1} for 20 min followed by relaxation for 2 h. The electrochemical properties of the full-cell, paired with a (Co,Fe)O@PDA-C-100 anode and an NCM811 cathode, were evaluated at various current densities ranging from 0.1 C to 5.0 C (1.0 C = 180 mA g^{-1}) over the voltage range of 0.5–4.2 V, with the NP ratio fixed at ~1.2.

3. Results and discussion

The (Co,Fe)O@PDA-C porous nanocages were synthesized through a straightforward two-step process (Scheme 1). In the first step, the CoFe-PBA nanocages were prepared by co-precipitation of cobalt (II) acetate tetrahydrate and trisodium citrate dihydrate with potassium hexacyanoferrate under ambient conditions (Scheme 1(a)). During this process, citrate ions served a dual role: controlling the release of Co^{2+} from Co-citrate complexes and acting as a directing agent to facilitate the formation of CoFe-PBA nanocages. In the second step, PDA coating layers were applied to the CoFe-PBA nanocages using a solution-based coating method. The resulting samples, labeled CoFe-PBA@PDA-20, CoFe-PBA@PDA-100, and CoFe-PBA@PDA-200, were coated with varying amounts of PDA before undergoing the Kirkendall diffusion effect. These labels represent the specific quantities of PDA applied to the CoFe-PBA template (e.g., PDA-20 indicates that 20 mg of PDA was used). In the first stage of the post-pyrolysis treatment, CoFe-PBA@PDA powders were transformed into PDA derived carbon coated nanocages containing metallic CoFe nanoparticles, denoted as (Co,Fe)@PDA-C, through carbonization in an N_2 atmosphere at 400 °C for 3 h. During this process, the PDA coating layer was converted into a carbon layer on the nanocage surface, while simultaneously, metallic CoFe nanoparticles were formed within the CoFe-PBA nanocage through carbothermic reduction. Moreover, the PDA-derived carbon inhibited the excessive crystal growth and agglomeration of metallic CoFe nanocrystals, resulting in (Co,Fe)@PDA-C composite nanocages containing nanoscale metallic CoFe nanoparticles uniformly distributed within carbon nanocages (Scheme 1(b)). In the second stage of the post-pyrolysis process, the (Co,Fe)@PDA-C composite nanocages were oxidized at 400 °C for 3 h, leading to the formation of (Co,Fe)O@PDA-C porous nanocage with hollow (Co,Fe)O nanoparticles via the Kirkendall diffusion mechanism (Scheme 1(c)). During this process, the PDA-derived carbon layer served as a heat source through combustion, facilitating an intimate reaction between the metallic CoFe nanocrystals and oxygen gas, thus effectively promoting the Kirkendall diffusion effect. The Kirkendall diffusion effect involves the movement of an interface between two elements due to differences in their diffusion rates. In this case, the Kirkendall diffusion effect occurred between the metallic CoFe and oxygen element played a critical role in forming the hollow (Co,Fe)O nanoparticles during the oxidation process (Scheme S1-① in Supplementary Information). Initially, a thin layer of (Co,Fe)O is formed on the surface of the CoFe nanoparticles, establishing a boundary between the metallic CoFe core and the (Co,Fe)O shell. As the oxidation proceeded, the outward diffusion of Co/Fe cations (Co^{2+} = 72 pm, Co^{3+} = 60 pm, Fe^{2+} = 76 pm, Fe^{3+} = 64 pm) was favored over the inward diffusion of oxygen gas (O^{2-} = 140 pm) due to their relatively smaller ionic radius and faster diffusion rates. Furthermore, Co cations diffused slightly faster than Fe cations due to the smaller ionic radius, resulting in cobalt oxide being located predominantly on the surface of the (Co,Fe)O shell (Scheme S1-②). This disparity in diffusion rates ultimately led to the formation of Kirkendall voids at the interface between the metallic CoFe nanocrystals and the surrounding (Co,Fe)O shell, contributing to the aggregating of pores within the nanocage structure (Scheme S1-③). Consequently, this Kirkendall diffusion process enabled the complete conversion of metallic CoFe nanocrystals into hollow (Co,Fe)O nanoparticles constructed by Fe_3O_4 and Co_3O_4 nanoparticles inside and on the surface of the shell (Scheme S1-④). During the oxidation process, the PDA-derived carbon was entirely combusted, yielding hollow (Co,Fe)O@PDA-C porous nanocages. The PDA-derived carbon

played a crucial role in forming hollow (Co,Fe)O nanoparticles during the synthesis of (Co,Fe)O@PDA-C porous nanocages. By combusting to CO_2 during oxidation, the PDA-derived carbon transferred thermal energy to the CoFe nanocrystals, thus influencing the oxidation rate of the metallic species. For instance, in the case of CoFe@PDA-C-20 nanocages, the small amount of PDA-derived carbon burned off rapidly during oxidation, providing relatively limited thermal energy to the metallic species, which resulted in shorter interaction times between the CoFe nanocrystals and oxygen. Consequently, (Co,Fe)O@PDA-C-20 porous nanocages containing smaller-sized (Co,Fe)O nanoparticles without hollow structures were formed. In contrast, the abundant PDA-derived carbon on (Co,Fe)@PDA-C-200 nanocages led to a more intense combustion reaction, prolonging the interaction time between the CoFe nanocrystals and oxygen. During the extended process, overgrown (Co,Fe)O crystals with denser and larger structures formed within the (Co,Fe)O@PDA-C-200 porous nanocages. The optimized PDA content in the (Co,Fe)@PDA-C-100 nanocages provided an ideal thermal balance, which ensured sufficient control over the oxidation rate while allowing the Kirkendall diffusion effect to effectively yield well-defined hollow (Co,Fe)O nanoparticles. In summary, (Co,Fe)O@PDA-C-100 porous nanocages, featuring hollow (Co,Fe)O nanoparticles, were successfully synthesized by optimizing the oxidation rate of Co/Fe nanocrystals through careful control of the PDA-derived carbon content. The hollow structure is anticipated to effectively accommodate the volumetric stress of (Co,Fe)O nanoparticles during lithiation/delithiation, while also enhancing the wettability of the electrolyte within the porous nanocage, thereby facilitating the diffusion of charged species through the nanostructures.

A comprehensive analysis of the morphology and crystallography of the prepared nanocages was conducted following each synthesis step to elucidate their formation mechanism. Fig. S1 in Supplementary Information illustrates the microstructure and X-ray diffraction (XRD) pattern of the CoFe-PBA nanocages obtained through the co-precipitation process. The field emission scanning electron microscopy (FE-SEM) image (Fig. S1(a)) demonstrates well-dispersed and non-agglomerated nanocages with an average diameter of approximately 600 nm. Furthermore, the rough surface of the nanocage structure (Fig. S1(b)) strongly suggests the successful formation of CoFe-PBA, indicating that the synthesized nanocages possess a porous structure with a uniform size distribution. This supports the conclusion that the co-precipitation process under ambient conditions effectively yields well-formed nanocages. A more detailed examination of the internal structure is provided by the transmission electron microscopy (TEM) image (Fig. S1(c)), which reveals the porous nature of the internal structure of the CoFe-PBA nanocages. The contrast variations in the TEM image highlight the presence of both dense regions and voids, further confirming the porous characteristics that were initially suggested by the FE-SEM images. The XRD pattern (Fig. S1(d)) displays sharp diffraction peaks corresponding to the crystalline phase of CoFe-PBA. In addition, a broad diffraction peak at $2\theta = 19.6°$ was detected, indicating the presence of an amorphous phase within the material. This coexistence of both crystalline and amorphous phases suggests a complex internal structure, which likely contributes to the porosity observed in the nanocages. The elemental mapping images (Fig. S1(e)) further confirm the elemental composition of the CoFe-PBA nanocages, demonstrating the uniform distribution of Fe, Co, C, and N elements throughout the structure. This uniform elemental distribution, combined with the structural analyses, highlights the effectiveness of the synthesis approach in producing nanocages with a well-defined porous morphology and homogeneous composition.

The characterization results of CoFe-PBA@PDA-100 nanocages coated with 100 mg of PDA on CoFe-PBA and (CoFe)@PDA-C-100 nanocages obtained after the carbonization process of these structures prior to inducing the Kirkendall diffusion effect are shown in Fig. 1. The FE-SEM image of CoFe-PBA@PDA-100 nanocages (Fig. 1(a)) prepared using a solution-based coating method exhibits a distinct nanocage morphology with average size of approximately 620 nm, slightly enlarging due to the PDA coating. The inset FE-SEM image in Fig. 1(a) reveals the smooth surface of CoFe-PBA@PDA-100 due to the uniform coating of PDA across the CoFe-PBA template. Subsequently, FE-SEM image of the (Co,Fe)@PDA-C-100 nanocages (Fig. 1(b)) obtained by carbonization of CoFe-PBA@PDA-100 in an inert atmosphere at 400 °C for 3 h exhibits identical morphology with similar size even after heating process, while the major difference is observed at an increase in surface roughness due to the formation of transition metal nanocrystals caused by the carbothermic reduction during heat treatment. Additionally, TEM images (Fig. 1(c, d)) reveal metallic CoFe nanoparticles with an average size of 10 nm embedded within nanocages uniformly coated by a PDA-derived carbon layer with a thickness of approximately 13 nm. The carbonaceous materials including the PDA-C coating layer and organic group in the PBA effectively suppress the overgrowth of nanocrystals, resulting in a dispersion of ultrafine nanocrystals within the nanocage. Furthermore, the high-resolution TEM (HR-TEM) image (Fig. 1(e)) shows a lattice spacing of 0.20 nm corresponding to the CoFe (110) plane, which aligns with the XRD pattern results in Fig. 1(f), further confirming the formation of CoFe nanocrystals. The elemental mapping images (Fig. 1(g)) demonstrate the uniform distribution of Co, Fe, C, and N within the (Co,Fe)@PDA-C-100 porous nanocages.

To apply the nanoscale Kirkendall diffusion mechanism, the porous nanocages underwent an oxidation process at 400 °C in an air atmosphere. The phase transformations occurring during oxidation influenced by varying concentrations of PDA ((Co,Fe)O@PDA-C-200, (Co,Fe)O@PDA-C-100, (Co,Fe)O@PDA-C-20, and (Co,Fe)O were investigated using XRD analysis, as shown in Fig. S2(a–d). In the XRD pattern of (Co,Fe)O without PDA-derived carbon (Fig. S2(a)), broad peaks corresponding to the Co_3O_4 and Fe_3O_4 phases were observed at $2\theta = 36°$, indicating a relatively low degree of crystallinity. However, as the PDA content increased, the diffraction peaks gradually merged into an asymmetric single peak, as shown in Fig. S2(b–d). This merging suggests an increase in the crystallinity of Co_3O_4 nanoparticles in close proximity to the PDA-derived carbon. This phenomenon can be attributed to the combustion of the PDA-derived carbon layer, which supplied prolonged thermal energy to the Co_3O_4 nanocrystals, thereby enhancing their crystallinity under identical heat treatment conditions. Additionally, peaks corresponding to K-species originating from the CoFe-PBA precursor were observed in the XRD results. These K-species could be remnants from the initial synthesis and reflect their incomplete removal during the process. The presence of K-species could potentially influence the phase stability and morphology of the resulting composite structure. The findings from the XRD analysis indicate that the presence of PDA-derived carbon plays a significant role in modulating the crystallinity and phase development of the (Co,Fe)O nanoparticles, ultimately impacting the structural and functional properties of the final composite materials.

The morphological changes of (Co,Fe)O@PDA-C-20, (Co,Fe)O@PDA-C-100, and (Co,Fe)O@PDA-C-200 porous nanocages obtained after the oxidation process are presented in Fig. S3, Fig. 2, and Fig. S4, respectively. Notably, the characterization of (Co,Fe)O@PDA-C-100 porous nanocages obtained by combustion of optimized PDA-C are shown in Fig. 2. The low-magnification FE-SEM images of the (Co,Fe)O@PDA-C-100 nanocages (Fig. 2(a)) demonstrate the nanocage morphology with an average diameter to approximately 550 nm without aggregation even after secondary heat treatment. Additionally, the high-magnification FE-SEM image (Fig. 2(b)) further illustrates that the oxidation

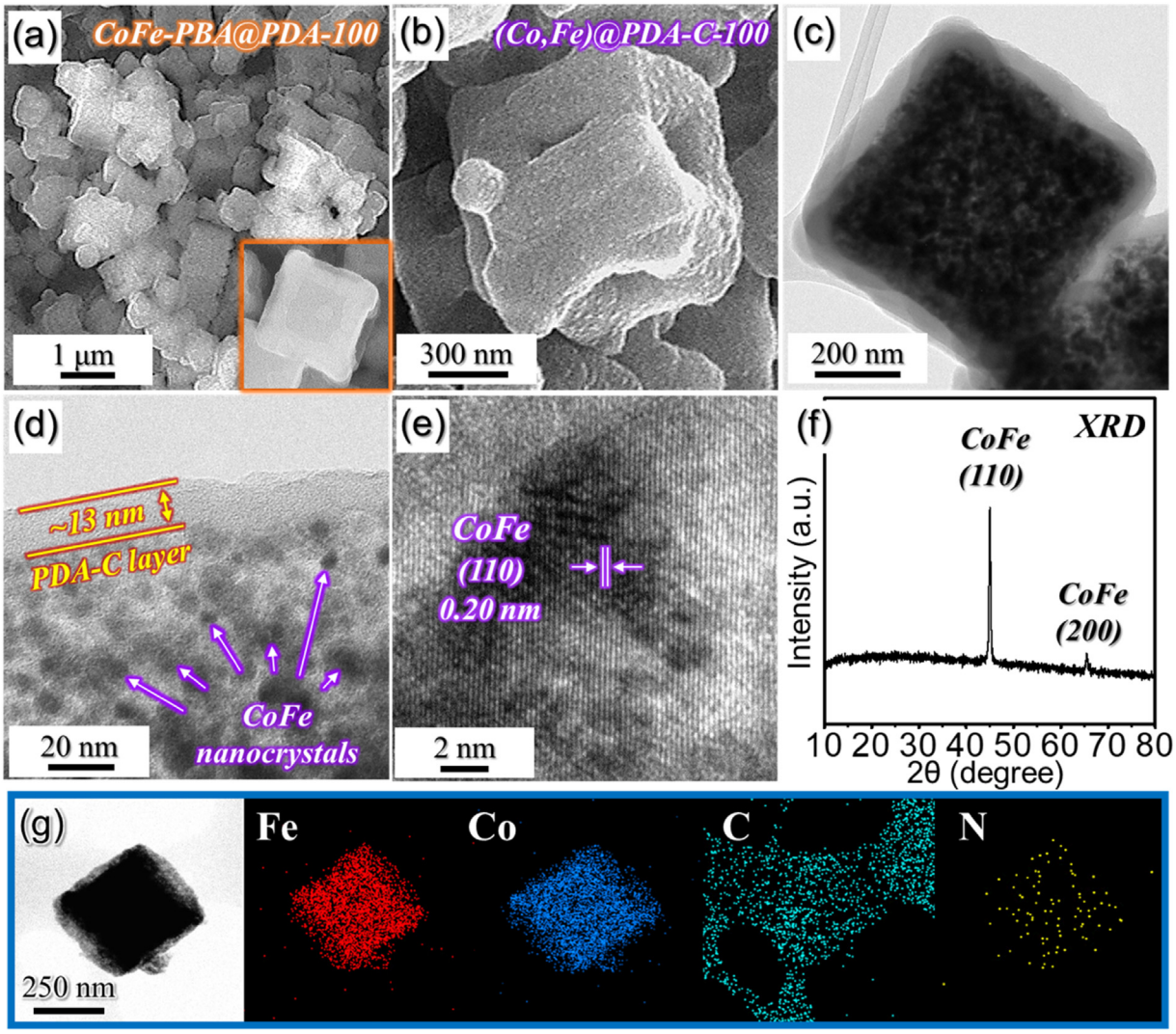

Fig. 1. (a) FE-SEM images of CoFe-PBA@PDA-100 nanocage, and morphologies, XRD pattern, and elemental mapping images of the (Co,Fe)@PDA-C-100 nanocages obtained after the carbonization at 400 °C for 3 h under N_2 atmosphere: (b) FE-SEM image, (c, d) TEM images, (e) HR-TEM image, (f) XRD pattern, and (g) elemental mapping images.

process has substantially influenced both the internal and external surfaces of the porous nanocages, resulting in morphological modifications. These FE-SEM observations are corroborated by TEM images shown in Fig. 2(c–e). The TEM image (Fig. 2(c)) reveals inward shrinkage resulting in the formation of a porous nanocage structure, attributed to the combustion of carbonaceous materials, including the organic ligand of PBA and PDA-derived carbon layer. The formation of hollow (Co,Fe)O nanoparticles within these porous nanocages through the Kirkendall diffusion effect is clearly depicted in Fig. 2(d), where multiple pores are visible within the nanocage structure. Furthermore, HR-TEM image (Fig. 2(e)) reveals the distribution of Co_3O_4 and Fe_3O_4 nanocrystals with an average size of 7 nm within the hollow (Co,Fe)O nanoparticles with an average size of 25 nm. Electron energy loss spectroscopy (EELS) mapping images (Fig. 2(e)) indicate a high concentration of Co element distributed along the surface of the hollow (Co,Fe)O shell, while Fe element is distributed predominantly in the inner part of the shell. This distribution is a result of the faster diffusion rate of Co cations, which have a relatively smaller ionic radius compared to Fe cations, during the oxidation process. Accordingly, the lattice spacing of 0.24 and 0.47 nm corresponding to the Fe_3O_4 (222) and Co_3O_4 (111) planes are observed inside and on the surface of the hollow (Co,Fe)O shell, respectively. Supporting these observations, the selected area electron diffraction (SAED) pattern (Fig. 2(f)) exhibits well-resolved diffraction rings corresponding to the crystal lattices of Fe_3O_4 and Co_3O_4. Additionally, the scanning transmission electron microscopy (STEM) images, EELS mapping, and EELS spectra of a single nanocrystal comprising the shell are shown in Fig. 2(g, h). The STEM images obtained with the $(1\bar{1}1)$ zone axis reveal the typical cubic crystal structure with the $Fd\bar{3}m$ space group corresponding to both Fe_3O_4 and Co_3O_4. EELS mapping images of the nanocrystal further demonstrate the separation of the Fe_3O_4 and Co_3O_4 phases. The EELS spectra of the regions marked by green and red circles indicate Co L_2, L_3 (green circle) and Fe L_2, L_3 (red circle) peaks indicating the Co^{2+}/Co^{3+} and Fe^{2+}/Fe^{3+} oxidation states in the Co_3O_4 and Fe_3O_4 crystal phases, respectively. Additionally, the Raman spectrum of the hollow (Co,Fe)O@PDA-C-100 porous nanocages (Fig. 2(i)) displays distinct peaks at 179, 281, 467, 518, and 668 cm^{-1}, which are characteristic of Co/Fe-O bonding [22,23]. Elemental mapping results in Fig. 2(j) illustrate the uniform distribution of Fe, Co, and O throughout the (Co,Fe)O@PDA-C-100 porous nanocage, with no observable carbon remaining. These results are consistent with the elemental analysis (EA) results in Table S1 in Supplementary Information, where negligible carbon content of approximately 0.9 wt.% was detected. This indicates that the PDA-derived carbon was fully combusted to

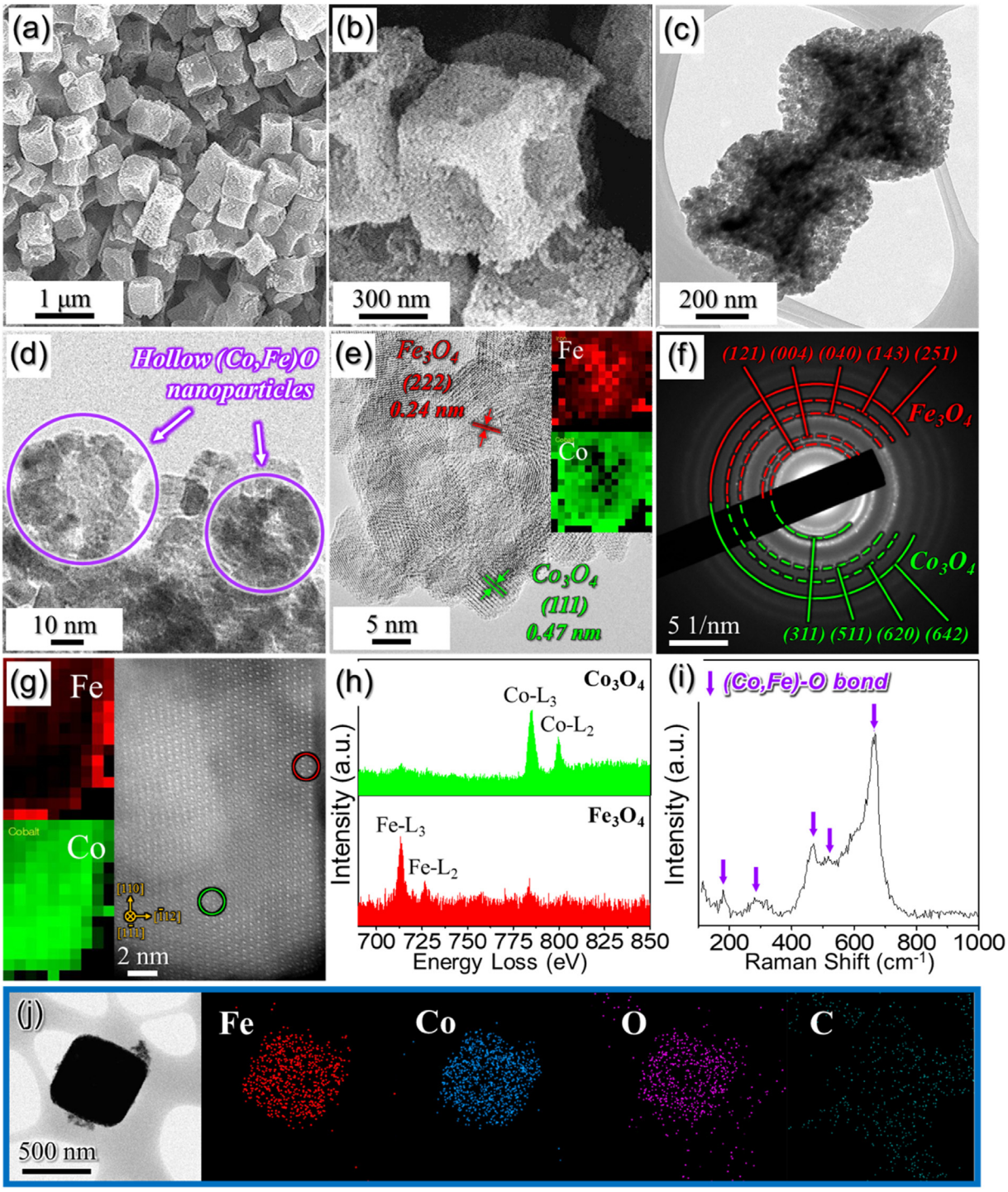

Fig. 2. Morphologies, EELS mapping images, STEM image, EELS spectra, Raman analysis, and elemental mapping images of the (Co,Fe)O@PDA-C-100 porous nanocages obtained after the carbonization followed by oxidation at 400 °C for 3 h: (a, b) FE-SEM images, (c, d) TEM images, (e) HR-TEM and EELS mapping images, (f) SAED pattern, (g) STEM and EELS mapping images, (h) EELS spectra, (i) Raman analysis, and (j) elemental mapping images.

CO_2, playing a sacrificial role in facilitating the Kirkendall diffusion effect. Moreover, to estimate the quantitative ratio of the crystal phases in the (Co,Fe)O@PDA-C-100 porous nanocage, TEM-energy-dispersive X-ray spectroscopy (TEM-EDS) and inductively coupled plasma optical emission spectroscopy (ICP-OES) analysis were performed (Fig. S5). Qualitative analysis of the nanostructure by TEM-EDS revealed the C, O, Fe, and Co elements, and residual K element originating from potassium hexacyanoferrate (III) used in the preparation of the Prussian blue analogue was also identified (Fig. S5(a)). This is in line with the XRD results indicating Co_3O_4, Fe_3O_4, and K_xO phases of (Co,Fe)O@PDA-C-100 porous nanocage (Fig. S2). Furthermore, the specific contents of Co, Fe, and K elements in (Co,Fe)O@PDA-C-100 porous nanocage were quantified as 62, 36, and 2 wt.% (100 wt.% equivalent; Fig. S5(b)) by ICP-OES analysis. The atomic ratio of Co and Fe elements based on the results was 3.2:2.0, which matches well with the molar ratio of Co and Fe-salts in the prepared co-precipitation solution. Based on the elemental analysis and ICP-OES results (Table S1 and Fig.

S5(b)), the estimated contents of Co_3O_4, Fe_3O_4, K_xO, and other residual organic elements in (Co,Fe)O@PDA-C-100 porous nanocage were 61, 36, 1, and 2 wt.%, respectively.

For a more comprehensive comparison, the morphological details of the (Co,Fe)O@PDA-C-20 and (Co,Fe)O@PDA-C-200 porous nanocages synthesized using the same methodology as the (Co,Fe)O@PDA-C-100 are presented in Figs. S3 and S4. The low- and high-magnification FE-SEM images of (Co,Fe)O@PDA-C-20 and (Co,Fe)O@PDA-C-200 nanocages (Figs. S3(a, b) and S4(a, b)) reveal uniform nanocage structures with an average size of approximately 550 nm, consistent with the size of (Co,Fe)O@PDA-C-100 (Fig. 2(a, b)). The TEM images of the (Co,Fe)O@PDA-C-20 and (Co,Fe)O@PDA-C-200 nanocages (Figs. S3(c) and S4(c)) also exhibit a porous structure similar to that of the (Co,Fe)O@PDA-C-100 nanocages (Fig. 2(c)). However, the TEM image of the (Co,Fe)O@PDA-C-20 porous nanocages (Fig. S3(d)) formed by combusting a smaller amount of PDA-derived carbon exhibits smaller (Co,Fe)O nanoparticles with an average size of approximately 6 nm and lacks a hollow structure. In contrast, the TEM image of (Co,Fe)O@PDA-C-200 porous nanocages (Fig. S4(d)) synthesized by burning a larger quantity of PDA-derived carbon demonstrates the presence of larger and denser (Co,Fe)O nanoparticles with an average size of approximately 20 nm. These observations indicate that the degree of oxidation in the nanocages is dependent on the content of carbonaceous materials. Notably, as the content of carbon increased, the more intense combustion reaction provided additional thermal energy to the metallic species, thereby promoting the growth of (Co,Fe)O crystals. Furthermore, the elemental mapping images of (Co,Fe)O@PDA-C-20 and (Co,Fe)O@PDA-C-200 porous nanocages (Figs. S3(e) and S4(e)) confirm the absence of carbon within the nanocages, while showing uniform distribution of Fe, Co, and O elements throughout the structures. This observation is in line with the elemental mapping images of the respective nanocages, and is further supported by the EA results (Table S1), which indicate negligible carbon content of approximately 1.1 and 0.7 wt.% for (Co,Fe)O@PDA-C-20 and (Co,Fe)O@PDA-C-200 nanocages, respectively. Additionally, the Raman spectra of the (Co,Fe)O@PDA-C-20 and (Co,Fe)O@PDA-C-200 nanocages (Fig. S6(a, b)) show peaks associated with Co/Fe-O bonds, which further support phase identification. These peaks are consistent with those observed for the hollow (Co,Fe)O@PDA-C-100 composite nanocages (Fig. 2(i)) [22,23], reinforcing the similarity in structural characteristics among the samples. The pore properties of the nanocages with different structural features based on controlling the PDA content were evaluated through N_2 adsorption-desorption isotherms and BJH pore size distribution as shown in Fig. S7. The (Co,Fe)O@PDA-C-20, (Co,Fe)O@PDA-C-100, and (Co,Fe)O@PDA-C-200 porous nanocages all exhibit similar isotherms, suggesting the mesoporous characteristics based on the CoFe-PBA template. Additionally, the BET specific surface areas of (Co,Fe)O@PDA-C-20, (Co,Fe)O@PDA-C-100, and (Co,Fe)O@PDA-C-200 porous nanocages recorded at 28.3, 44.1, and 46.7 $m^2\ g^{-1}$, respectively (Fig. S7(a, c, e)). Notably, the specific surface area of the hollow (Co,Fe)O@PDA-C-100 porous nanocages increased significantly to 44.1 $m^2\ g^{-1}$ compared to the (Co,Fe)O@PDA-C-20 (28.3 $m^2\ g^{-1}$), strongly supporting the formation of hollow (Co,Fe)O nanoparticles through the Kirkendall diffusion effect. In the case of (Co,Fe)O@PDA-C-200, it showed a slightly higher specific surface area (46.7 $m^2\ g^{-1}$) than the (Co,Fe)O@PDA-C-100 porous nanocage. This is due to the intense combustion reaction between CoFe nanocrystals and oxygen, which resulted in the formation of larger (Co,Fe)O particles and enlarged interparticle voids. This trend is further evidenced by the increased average pore diameters in the BJH pore size distribution as 12.6, 15.9, and 17.8 nm, respectively (Fig. S7(b, d, f)).

The chemical environments and bonding states of various elements in the hollow (Co,Fe)O@PDA-C-100 porous nanocages obtained by optimization of synthesis conditions were characterized by XPS analysis. The XPS survey spectrum depicted in Fig. S8 revealed evident photoelectron signals related to Co 2*p*, Fe 2*p*, O 1*s*, K 2*p*, and C 1*s* [24,25]. The Co 2*p* spectrum displayed in Fig. 3(a) exhibited well-defined peaks corresponding to the Co $2p_{3/2}$ and Co $2p_{1/2}$ orbitals, along with two shake-up satellite peaks marked as "Sat". The deconvoluted spectrum showcased distinct peaks at binding energies of 781.9 eV (Co $2p_{3/2}$) and 796.5 eV (Co $2p_{1/2}$), attributed to the presence of Co^{2+} species within the Co_3O_4 structure [26,27]. Additional peaks at binding energies of 779.6 eV (Co $2p_{3/2}$) and 794.7 eV (Co $2p_{1/2}$) were assigned to the Co^{3+} species in the porous nanocages [28]. Furthermore, two shake-up satellite peaks corresponding to the Co 2*p* signal indicated the presence of anti-bonding orbitals between the Co and O atoms [29]. Similarly, the Fe 2*p* spectrum illustrated in Fig. 3(b) displayed distinct peaks corresponding to the Fe $2p_{3/2}$ and Fe $2p_{1/2}$ orbitals, along with two shake-up satellite peaks marked as "Sat". The deconvoluted spectrum revealed well-defined peaks at binding energies of 711.8 eV (Fe $2p_{3/2}$) and 725.4 eV (Fe $2p_{1/2}$), assigned to the Fe^{2+} species within the Fe_3O_4 nanocrystals [30,31]. Additional peaks at binding energies of 709.5 eV (Fe $2p_{3/2}$) and 723.3 eV (Fe $2p_{1/2}$) were attributed to the Fe^{3+} species occurring in the porous nanocages [32,33]. Furthermore, two shake-up satellite peaks within the Fe 2*p* signal indicated the presence of anti-bonding orbitals between the Fe and O atoms [34,35]. Additionally, the high-resolution O 1*s* spectrum (Fig. 3(c)) could be fitted into three peaks at binding energies of 528.6, 529.8, and 530.7 eV corresponding to Co–O/Fe–O, C–O/C=O, and C–OH bonds, respectively [7]. The high-resolution C 1*s* spectrum depicted in Fig. 3(d) exhibits three peaks of low intensity at binding energies of 284.1, 285.4, and 288.4 eV, corresponding to C=C, C–N/C–C, and C–O bonds, respectively [29,36]. The C=C peak indicates that graphitic carbon had been generated due to the graphitization catalytic effect of CoFe nanocrystals during the carbonization process [37]. Additionally, the C–N peak originating from the conversion of PDA and –C≡N– groups in PBA to the N-doped C is confirmed [29,38]. However, the weak signal of the peaks demonstrates the combustion of most of the carbon species during the oxidation process. Aside from the C 1*s* signals, two strong peaks at higher binding energies (>290 eV) correspond to K $2p_{3/2}$ and K $2p_{1/2}$, indicating the presence of residual K-species derived from CoFe-PBA [39].

To demonstrate the structural and electrochemical advantages of the porous nanocages prepared by controlling the carbon coating on PBA templates, PDA-C-free (Co,Fe)O nanocages and Co/Fe-salts derived bare (Co,Fe)O nanocrystals were synthesized using an identical two-step heat treatment, and their morphological analysis are presented in Fig. S9. The morphological characteristics of the PDA-C-free (Co,Fe)O nanocages obtained through direct two-step heat treatments of CoFe-PBA templates are illustrated in Fig. S9(a–c). The FE-SEM images of the (Co,Fe)O nanocages (Fig. S9(a, b)) exhibit well-defined and non-agglomerated structures with an average size of approximately 550 nm. This morphology is comparable to that of the other porous nanocages ((Co,Fe)O@PDA-C-20, (Co,Fe)O@PDA-C-100, (Co,Fe)O@PDA-C-200) synthesized using PDA-coated CoFe-PBA templates. In contrast to these porous nanocages with more crystallized nanoparticles due to oxidation facilitated by the combustion of PDA-derived carbon, the PDA-C-free (Co,Fe)O nanocages contain ultrafine (Co,Fe)O nanoparticles with an average width of 5 nm, as evidenced by the TEM image (Fig. S9(c)). This is further supported by the XRD pattern in Fig. S2, where the broad peaks of the PDA-C-free (Co,Fe)O nanocages indicate low crystallinity corresponding to Co_3O_4 and Fe_3O_4 phases. Elemental mapping images (Fig. S9(d)) demonstrate the uniform distribution of Fe, Co, and O throughout the nanocages derived from CoFe-PBA, confirming the consistent dispersion of the ultrafine (Co,Fe)O nanoparticles within the nanostructure. On the other

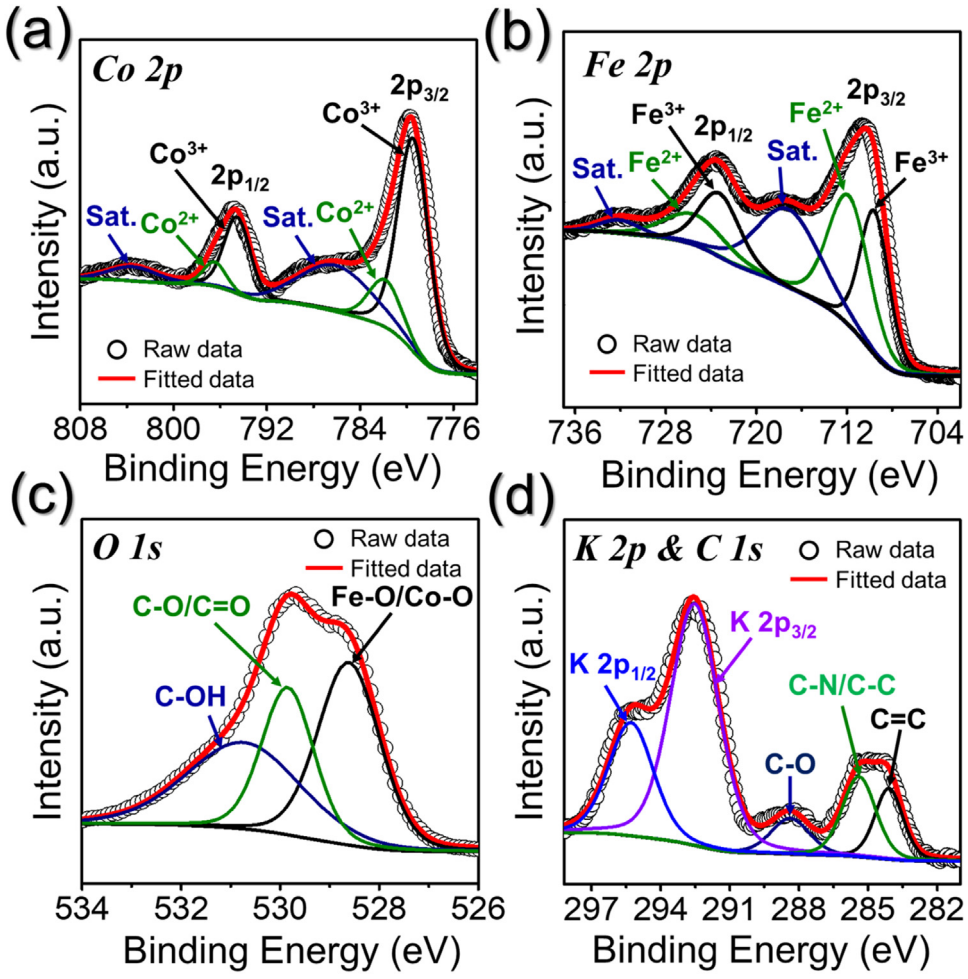

Fig. 3. Core level XPS spectra of (Co,Fe)O@PDA-C-100 porous nanocages: (a) Co 2*p*, (b) Fe 2*p*, (c) O 1*s*, and (d) K 2*p* & C 1*s*.

hand, bare (Co,Fe)O crystals synthesized by physical grinding and heat treatments of the metal precursors display irregular sizes and significant agglomeration of metal oxide particles, as shown in Fig. S9(e, f). This agglomeration is attributed to the absence of an organic scaffold from the CoFe-PBA preventing particle growth during heating. Furthermore, the XRD pattern in Fig. S9(g) reveals diffraction peaks predominantly associated with Co_3O_4 and Fe_3O_4 phases, with no detectable peaks corresponding to K-species from the CoFe-PBA, indicating the purity of the synthesized metal oxides.

The electrochemical characteristics of the hollow (Co,Fe)O@PDA-C-100 porous nanocages serving as anodes for LIBs are compared with those of (Co,Fe)O@PDA-C-20, (Co,Fe)O@PDA-C-200, (Co,Fe)O nanocages, and bare (Co,Fe)O nanocrystals (Fig. 4). The CV plots for the initial five cycles of these electrodes are shown in Figs. 4(a) and S10(a–d), obtained with a scan rate of 0.1 mV s^{-1} within a voltage range of 0.001 to 3.0 V. In the initial cathodic sweep, the hollow (Co,Fe)O@PDA-C-100 porous nanocages exhibit a sharp reduction peak at approximately 0.62 V indicating the formation of a solid electrolyte interface (SEI) on the surfaces and interfaces of the electrode, as well as the conversion reaction between Co_3O_4/Fe_3O_4 and Li^+ leading to the formation of metallic Co/Fe and Li_2O [40–42]. Similarly, the (Co,Fe)O@PDA-C-20, (Co,Fe)O@PDA-C-200, (Co,Fe)O nanocages, and bare (Co,Fe)O nanocrystals display reduction peaks at around 0.61 V during the initial cathodic sweep, attributed to the identical reaction. These sharp reduction peaks in the CV curves correspond to the dominant voltage plateaus observed at approximately 0.6 V in the initial discharge curves for all anodes (Fig. 4(b)). From the second cycle onwards, broad cathodic peaks appear at approximately 1.52 and 0.81 V in all samples—(Co,Fe)O@PDA-C-20, (Co,Fe)O@PDA-C-100, (Co,Fe)O@PDA-C-200, (Co,Fe)O nanocages, and bare (Co,Fe)O nanocrystals (Figs. 4(a) and S10(a–d)). These broad peaks are associated with the Li^+ insertion into Co_3O_4/Fe_3O_4 and the continued conversion reaction between $Li_xCo_3O_4/Li_xFe_3O_4$ and Li^+, leading to the formation of metallic Co/Fe and Li_2O [42–44]. During the anodic sweep, oxidation peaks are observed at approximately 1.1, 1.6, and 2.1 V in the (Co,Fe)O@PDA-C-20, (Co,Fe)O@PDA-C-100, (Co,Fe)O@PDA-C-200, (Co,Fe) nanocages, and bare (Co,Fe)O nanocrystals, respectively. These peaks are attributed to the oxidation of metallic Co/Fe to Co_3O_4/Fe_3O_4 and the decomposition of Li_2O [40–44]. Moreover, the strong overlap of the CV profiles from the second cycle onwards in the hollow (Co,Fe)O@PDA-C-100 porous nanocages obtained by nanoscale Kirkendall diffusion indicates reversible reactions, contributing to superior cycling stability. Additionally, to further investigate the Li-ion storage mechanism for the (Co,Fe)O@PDA-C-100 anodes, in-situ XRD analysis for the anode in the initial cycle was performed (Fig. S11). During the in-situ XRD analysis, the (Co,Fe)O@PDA-C-100 anode was slowly cycled at a current density of 0.1 A g^{-1} in a voltage range from 0.001 to 3.0 V. The XRD pattern of the (Co,Fe)O@PDA-C-100 anode in the initial step revealed two major diffraction peaks corresponding to the (220) and (311) planes of Co_3O_4 and Fe_3O_4 at approximately 30.6° and 36.3°, respectively.

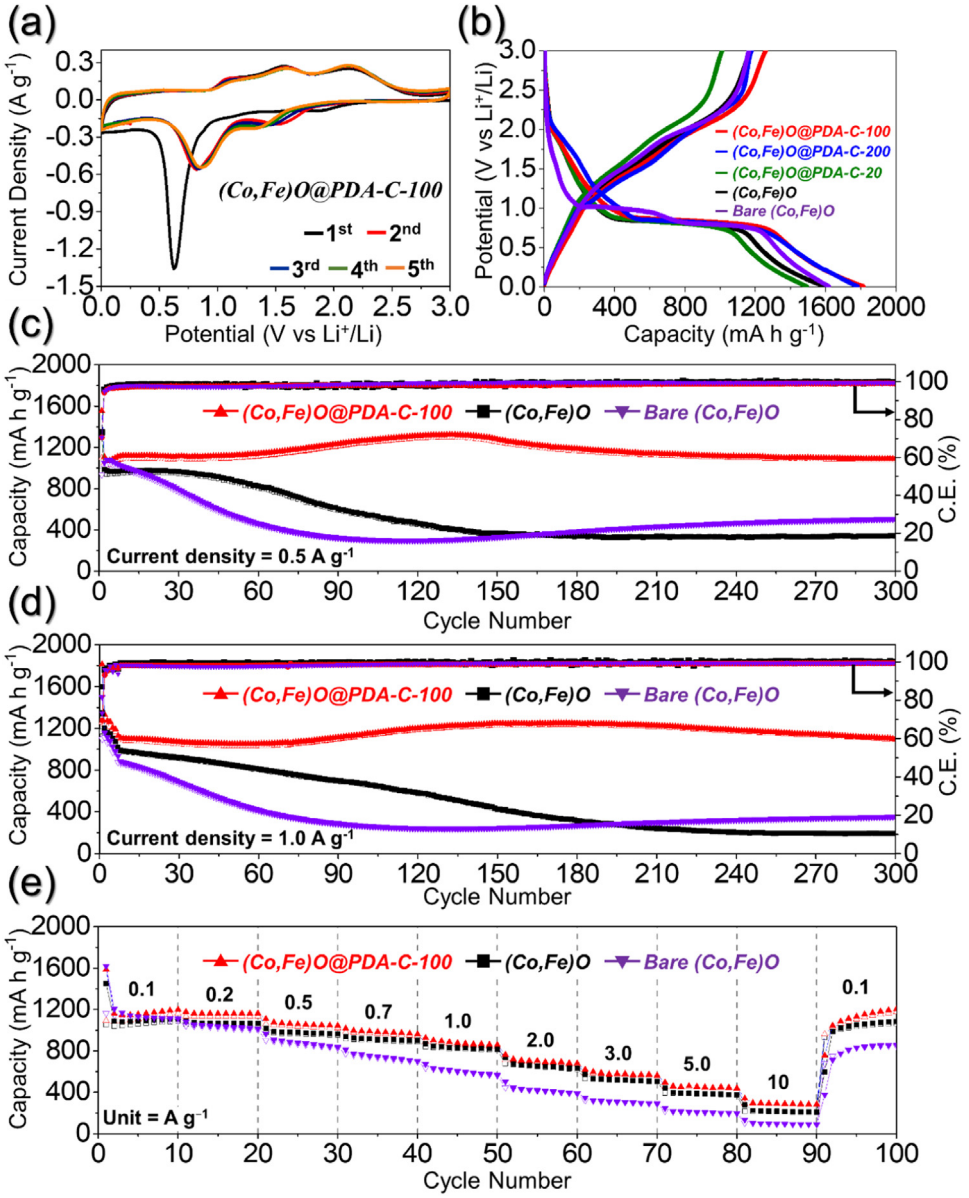

Fig. 4. Electrochemical properties of (Co,Fe)O@PDA-C-100, (Co,Fe)O porous nanocages, and bare (Co,Fe)O nanocrystals for Li-ion storage: (a) CV curves of (Co,Fe)O@PDA-C-100 porous nanocages, (b) initial discharge/charge curves at a constant current density of 0.1 A g^{-1}, cycle performances at current density of (c) 0.5 A g^{-1}, and (d) 1.0 A g^{-1}, and (e) rate performances.

During the discharge process reaching at 1.0 V, the two diffraction peaks gradually shifted to a lower angle, suggesting the formation of $Li_xCo_3O_4$ and $Li_xFe_3O_4$ intermediates by the reaction of Co_3O_4 and Fe_3O_4 with Li [42–44]. When discharged to 0.001 V after a voltage plateau of 0.9 V, the two diffraction peaks disappeared, and a peak corresponding to Li_2O appeared at 33.5°. This indicates that the conversion-based Co_3O_4 and Fe_3O_4 reduced to metallic Co and Fe through the further reaction of the $Li_xCo_3O_4$ and $Li_xFe_3O_4$ intermediates with Li [42–44]. In contrast, the Li_2O peak gradually disappeared during the charge process, and broad peaks with low intensity reappeared corresponding to the (220) and (311) planes of Co_3O_4 and Fe_3O_4. This observation demonstrates the formation of the amorphous and ultrafine crystals during the cycling. Based on the above discussion, the complete reaction mechanisms involved in the discharge and charge processes of the (Co,Fe)O@PDA-C-100 anodes are summarized below:

For the discharge and charge process:

$$Fe_3O_4 + xLi^+ + xe^- \leftrightarrow Li_xFe_3O_4 \quad (1)$$

$$Co_3O_4 + xLi^+ + xe^- \leftrightarrow Li_xCo_3O_4 \quad (2)$$

$$Li_xFe_3O_4 + (8-x)Li^+ + (8-x)e^- \leftrightarrow 3Fe + 4Li_2O \quad (3)$$

$$Li_xCo_3O_4 + (8-x)Li^+ + (8-x)e^- \leftrightarrow 3Co + 4Li_2O \quad (4)$$

The assembled cells were subjected to galvanostatic discharge/charge processes in order to assess their structural advantages. The initial discharge/charge profiles, shown in Fig. 4(b), were observed for all the prepared composites at a current density of 0.1 A g^{-1}. These voltage profiles align with the CV results, indicating distinct charge and discharge plateaus at

2.1 and 0.81 V, respectively. The initial discharge/charge capacities of (Co,Fe)O@PDA-C-20, (Co,Fe)O@PDA-C-100, (Co,Fe)O@PDA-C-200, (Co,Fe)O nanocages, and bare (Co,Fe)O nanocrystals were 1492/1011, 1814/1259, 1781/1180, 1599/1171, and 1618/1164 mA h g^{-1}, respectively, accompanied by corresponding initial Coulombic efficiency (ICE) values of 67.8%, 69.4%, 66.3%, 73.2%, and 71.9%. Notably, the hollow (Co,Fe)O@PDA-C-100 porous nanocages displayed a higher ICE compared to the (Co,Fe)O@PDA-C-20 and (Co,Fe)O@PDA-C-200 nanocages. This distinction is attributed to the Kirkendall voids of the hollow (Co,Fe)O@PDA-C-100 porous nanocages, enhancing the Li-ion diffusion and reducing irreversible reactions during the initial cycles.

The cycle performances of (Co,Fe)O@PDA-C-20, (Co,Fe)O@PDA-C-100, (Co,Fe)O@PDA-C-200, (Co,Fe)O porous nanocages, and bare (Co,Fe)O nanocrystals as anodes for LIBs at the current density of 0.5 and 1.0 A g^{-1} are shown in Figs. 4(c, d) and S12(a, b), respectively. The cell utilizing the (Co,Fe)O@PDA-C-100 porous nanocages exhibited stable and superior cycle performance at each current density compared to (Co,Fe)O@PDA-C-20, (Co,Fe)O@PDA-C-200, (Co,Fe)O, and bare (Co,Fe)O anodes. For instance, the (Co,Fe)O@PDA-C-100 porous nanocages showed a discharge capacity of 1098 mA h g^{-1} at a current density of 0.5 A g^{-1} (Fig. 4(c)). The discharge capacity of (Co,Fe)O@PDA-C-100 porous nanocages stabilized at 1090 mA h g^{-1} after 300 cycles, indicating a capacity retention of 99.3% with a low average capacity decay rate of 0.0025% per cycle. In addition, the cells using the (Co,Fe)O@PDA-C-20, (Co,Fe)O@PDA-C-200, and (Co,Fe)O anodes exhibited initial discharge capacities of 891, 1086, and 970 mA h g^{-1}, respectively, subsequently, the discharge capacities of those anodes stabilized at 739 (retention = 82.9%), 838 (retention = 77.2%), and 343 mA h g^{-1} (retention = 35.3%) after 300 cycles, indicating a decrease in capacity over extended cycling. Furthermore, the (Co,Fe)O@PDA-C-100 porous nanocages demonstrated higher CE value of 99.8% among all other nanocages (CE values of 99.5%, 99.2%, and 99.1% for (Co,Fe)O@PDA-C-20, (Co,Fe)O@PDA-C-200, and (Co,Fe)O anodes, respectively) after 300 cycles, indicating highly reversible electrochemical performance in the assembled cells. This can be attributed to the interconnected hollow porous structure, effectively mitigating volume changes during charge and discharge processes. In contrast, the cell using the bare (Co,Fe)O anode exhibited a discharge capacity of 1051 mA h g^{-1}, which significantly decreased to 507 mA h g^{-1} after 300 cycles.

At a higher current density of 1.0 A g^{-1} (Figs. 4(d) and S12(b)), similar capacity trends were observed during cycling. The cells utilizing the (Co,Fe)O@PDA-C-20, (Co,Fe)O@PDA-C-100, (Co,Fe)O@PDA-C-200, and (Co,Fe)O anodes had discharge capacities of 926, 1130, 1000, and 1021 mA h g^{-1}, respectively. Notably, the capacity contribution of the Co_3O_4 and Fe_3O_4 in the total capacity of (Co,Fe)O@PDA-C-100 was calculated to be 71% and 29% at current densities of 1.0 A g^{-1} based on the quantitative analysis (Fig. S5(b)) and the cycling test results of Fe-PBA-derived Fe_3O_4 (Fig. S13). The discharge capacity of (Co,Fe)O@PDA-C-100 anode stabilized at 1098 mA h g^{-1} after the 300th cycle (capacity retention of 97.2%), while the (Co,Fe)O@PDA-C-20, (Co,Fe)O@PDA-C-200, and (Co,Fe)O anodes exhibited discharge capacities of 407, 681, and 193 mA h g^{-1} (capacity retentions of 44.0%, 68.1%, and 18.9%), respectively. In contrast, the cell that used the bare (Co,Fe)O anode exhibited an initial discharge capacity of 933 mA h g^{-1}, even decreased significantly to 240 mA h g^{-1} after the 130th cycle. This most drastic decline can be attributed to the structural instability caused by the high crystallinity of the anode material during cycling. These observations highlight the detrimental impact of the non-porous structure and bulky crystal of bare (Co,Fe)O on its cycling performance. Notably, the gradual increase of discharge capacities for (Co,Fe)O@PDA-C-100 porous nanocages was confirmed for reaching 1323 and 1249 mA h g^{-1} at the 130th and 170th cycles at current densities of 0.5 and 1.0 A g^{-1}, respectively. This phenomenon has been previously reported for metal oxide electrodes over extended cycling periods [42,45–50]. Primarily, this phenomenon results from the formation of an organic polymer or gel-like solid electrolyte interphase (SEI) layer on the electrode surface due to the decomposition of the electrolyte [42,45–47]. This SEI layer can enhance the mechanical cohesion of the active material without hindering Li-ion transport. Additionally, this SEI layer could further enhance the reversible capacity by providing additional Li-ion storage sites through a pseudo-capacitive mechanism, notably in the low-potential region. Moreover, it is associated with a transformation of the crystalline structure to a more stable amorphous-like structure during prolonged cycling [42,48,49]. This transformation can increase the surface area of the structure, exposing more active sites for Li-storage, and improve structural stability, which contributes to the gradual enhancement in capacity over extended cycling. Finally, metallic Co/Fe nanoparticles irreversibly generated during the initial cycling enhance the overall conductivity of the electrode, which in turn improves charge transfer kinetics, thereby contributing to an increase in capacity during subsequent cycles [42,50]. These factors can contribute to the (Co,Fe)O@PDA-C-100 anode achieving a higher specific capacity than the theoretical specific capacity of 904 mA h g^{-1} estimated based on quantitative analysis results and theoretical specific capacities of 890 and 926 mA h g^{-1} for Co_3O_4 and Fe_3O_4, respectively, as previously reported [51,52]. Furthermore, the excellent cycling stability of the hollow (Co,Fe)O@PDA-C-100 porous nanocages can be attributed to several structural advantages. Firstly, the porous structure derived from PBA template facilitates the smooth Li-ion diffusion by enhancing electrode wetting and facilitating electrolyte percolation. Secondly, the hollow structure comprising small-sized nanoparticles *via* the Kirkendall diffusion effect enables them to accommodate substantial volumetric deformations during extended cycling, improving structural robustness. The relatively improved cycling performance of the (Co,Fe)O@PDA-C-20, (Co,Fe)O@PDA-C-200, and (Co,Fe)O nanocages can be attributed to the porous structure of the nanocages derived from the PBA template constructed by well-defined (Co,Fe)O particles. In contrast, bare (Co,Fe)O forms bulky crystals, which prevent it from accommodating significant volume changes during repeated Li-ion insertion processes. This results in structural deterioration and substantial capacity decay.

Rate capability tests were conducted across various current densities ranging from 0.1 A g^{-1} to 10 A g^{-1} to evaluate the performance of (Co,Fe)O@PDA-C-20, (Co,Fe)O@PDA-C-100, (Co,Fe)O@PDA-C-200, (Co,Fe)O, and bare (Co,Fe)O anodes. These tests aimed to further validate the structural advantages of these anodes (Figs. 4(e) and S12(c)). The hollow (Co,Fe)O@PDA-C-100 porous nanocages exhibited discharge capacities of 1200, 1162, 1043, 962, 859, 681, 563, 441, and 284 mA h g^{-1} at the 10th cycle under current densities of 0.1, 0.2, 0.5, 0.7, 1.0, 2.0, 3.0, 5.0, and 10 A g^{-1}, respectively. These capacities surpassed those of (Co,Fe)O@PDA-C-20, (Co,Fe)O@PDA-C-200, (Co,Fe)O, and bare (Co,Fe)O anodes. The discharge capacities of the (Co,Fe)O@PDA-C-20 and (Co,Fe)O@PDA-C-200 anodes were 1240/1214, 1142/1196, 949/1081, 831/969, 726/804, 571/540, 470/393, 367/256, and 225/105 mA h g^{-1} at identical current densities, respectively. The (Co,Fe)O@PDA-C-20 porous nanocage showed slightly lower discharge capacity than (Co,Fe)O@PDA-C-100 due to the absence of the hollow structure, while (Co,Fe)O@PDA-C-200 porous nanocage revealed the lowest rate properties by the non-hollow structure as well as large crystal size, lengthening the Li-ion diffusion length. The (Co,Fe)O@PDA-C-100 porous nanocage demonstrated enhanced rate performance compared to the other nanocages, which can be attributed to more efficient electrolyte penetration and a shorter ionic diffusion length due to the hollow structure. In comparison, the (Co,Fe)O and bare (Co,Fe)O anodes exhibited discharge capacities of 1109/1111,

1066/1016, 965/839, 899/705, 818/569, 630/391, 509/292, 378/197, and 209/89 mA h g^{-1} at identical current densities, respectively. It is well known that a smaller size of active material facilitates Li-ion diffusion, thereby enhancing the electrochemical redox kinetics [9,16,17]. Therefore, the (Co,Fe)O nanocages comprising nanocrystals with a relatively small size of 5 nm exhibited comparable rate characteristics similar to the (Co,Fe)O@PDA-C-100 anode. The discharge capacities of the (Co,Fe)O@PDA-C-100 anode obtained in the rate test were slightly different from the results of the cycle performance obtained at the current density of 1.0 A g^{-1}, which was attributed to the different active material loading masses. As a result of comparing the rate and cycling results based on the normal capacity (Unit = mA h), the discharge capacities of the rate and cycling tests at the 45th cycle corresponding to a current density of 1.0 A g^{-1} were almost identical (Fig. S14). The hollow (Co,Fe)O@PDA-C-100 porous nanocages demonstrated exceptional capacity retention and rate capability when the current density was reverted back to 0.1 A g^{-1}. The substantial discharge capacity, especially under high current densities, solidifies the structural superiority of the (Co,Fe)O@PDA-C-100 anode over (Co,Fe)O@PDA-C-20, (Co,Fe)O@PDA-C-200, (Co,Fe)O, and bare (Co,Fe)O anodes. The lowest discharge capacity observed in the bare (Co,Fe)O anode at a high current density of 10 A g^{-1} can be attributed to its non-porous structure and the formation of bulky crystals. In contrast, the well-defined porous structures of the (Co,Fe)O@PDA-C-100 nanocages facilitate effective electrode wetting, promoting fast redox reactions during electrochemical process. Furthermore, the tiny size of nanocrystals (approximately 7 nm) constructing the hollow structure reduces the diffusion length of Li-ion into the crystal structure, promoting the rapid transfer of charge species. Additionally, the electrochemical performance of (Co,Fe)O@PDA-C-100 porous nanocages prepared in this study is compared with other previously reported oxide-based anodes in Table S2, demonstrating superior high-rate capability and cycling stability. Furthermore, the synthesis process of these nanocages is both energy-efficient and cost-effective, highlighting their potential for large-scale production in battery applications.

To gain a deeper understanding of the electrochemical kinetics within the cell, CV curves were recorded for (Co,Fe)O@PDA-C-20, (Co,Fe)O@PDA-C-100, (Co,Fe)O@PDA-C-200, (Co,Fe)O, and bare (Co,Fe)O anodes. These curves were recorded at sweep rates ranging from 0.1 to 2.0 mV s^{-1}, as shown in Fig. S15(a), Fig. 5(a), Fig. S16(a), and Fig. S17(a, c). Following this, power law equations were used to analyze the relationship between peak current (i) and scan rates (ν). The goal of this analysis was to differentiate between capacitive and diffusion-controlled mechanisms observed in the CV curves [53,54].

$$i = a\nu^{b} \tag{5}$$

$$\log(i) = \log(a) + b\log(\nu) \tag{6}$$

Here, the parameters a and b are crucial in determining whether the mechanism operates under capacitive or diffusion-controlled dynamics. A b-value close to 0.5 indicates a diffusion-controlled mechanism, while b-value approaching 1 suggests capacitive control [53,54]. The b-values were derived from the slopes observed in log (i) vs. log (ν) plots for various anodic and cathodic peaks. These calculated b-values correspond to different redox peaks of the (Co,Fe)O@PDA-C-20, (Co,Fe)O@PDA-C-100, (Co,Fe)O@PDA-C-200, (Co,Fe)O porous nanocages, and bare (Co,Fe)O nanocrystals illustrated in Fig. S15(b), Fig. 5(b), Fig. S16(b), and Fig. S17(b, d). For the hollow (Co,Fe)O@PDA-C-100 porous nanocages, the b-values obtained for different redox peaks were 0.87, 0.79, 0.92, and 0.89, indicating a capacitive-dominant mechanism (Fig. 5(b)). Similar trends were observed in the (Co,Fe)O@PDA-C-20, (Co,Fe)O@PDA-C-200, (Co,Fe)O nanocages, and bare (Co,Fe)O nanocrystals. This similarity suggests that there are abundant pseudocapacitive reaction sites across these materials. However, the hollow (Co,Fe)O@PDA-C-100 porous nanocages displayed higher b-values compared to the (Co,Fe)O@PDA-C-20, (Co,Fe)O@PDA-C-200, (Co,Fe)O nanocages, and bare (Co,Fe)O nanocrystals. This difference is attributed to the interconnected porous network within the hollow structure, which effectively reduces the diffusion length of Li-ions and enhances the electrode-electrolyte contact. This, in turn, promotes a higher degree of surface-capacitive reactions. Additionally, the amount of surface-capacitive and diffusion-controlled reactions were quantitatively differentiated using the following equation [28,53,55]:

$$i = k_1\nu + k_2\nu^{1/2} \tag{7}$$

In this analysis, $k_1\nu$ and $k_2\nu^{1/2}$ signify the capacitive and diffusion contributions, respectively, while k_1 and k_2 are constants derived from the slope and intercept of $i(V)/\nu^{1/2}$ versus $\nu^{1/2}$ plot [28,53,55]. As depicted in Fig. 5(c), for hollow (Co,Fe)O@PDA-C-100 porous nanocages highlighted in red, the capacitive contribution factor ($k_1\nu$) reaches 82% at the scan rate of 2.0 mV s^{-1}. This observation indicates the consistently more capacitive contribution across various scan rates, as evident in Fig. 5(d). Similarly, the (Co,Fe)O@PDA-C-20, (Co,Fe)O@PDA-C-200, (Co,Fe)O nanocages, and bare (Co,Fe)O nanocrystals also demonstrate a higher percentage of capacitive processes, reaching 77%, 83%, 76%, and 62%, even at higher sweep rates (Figs. S15(c, d), Fig. S16(c, d), and Fig. 5(e–h)). These findings support the presence of rapid Li-ion transport kinetics in hollow (Co,Fe)O@PDA-C-100 porous nanocages, facilitated by several factors including better electrolyte penetration within the porous structure, the effective mitigation of volume changes during cycling, and the synergistic effects of the hollow and porous structure, collectively enabling fast charge transfer.

EIS (Fig. 6) confirmed that the hollow (Co,Fe)O@PDA-C-100 porous nanocages have rapid and stable Li-ion storage performance, unlike the (Co,Fe)O@PDA-C-20, (Co,Fe)O@PDA-C-200, (Co,Fe)O nanocages, and bare (Co,Fe)O nanocrystals. Nyquist plots of the electrode materials were obtained before cycling and after the 5th and 300th cycles at fully charged states. These plots were analyzed using the Randles-type equivalent circuit shown in Fig. S18, and the fitted values are summarized in Table S3. The Nyquist plots of the fresh cells (Fig. 6(a)) showed slightly varying electrolyte resistance (R_s) values ranging from 20 Ω to 47 Ω, indicating minor differences in electrode-electrolyte interface reactions. Additionally, the charge transfer resistance (R_{ct}) values for the (Co,Fe)O@PDA-C-20, (Co,Fe)O@PDA-C-100, (Co,Fe)O@PDA-C-200, (Co,Fe)O nanocages, and bare (Co,Fe)O nanocrystals were found to be 259, 221, 225, 261, and 297 Ω, respectively (Fig. 6(a)). It is worth noting that the hollow (Co,Fe)O@PDA-C-100 porous nanocages exhibited slightly lower R_{ct} compared to other electrodes due to the hollow structure formed by the Kirkendall diffusion effect. This structure shortens the path for charged species, effectively reducing resistance and improving charge transfer kinetics. However, after 5 cycles, a significant decrease in R_{ct} ((Co,Fe)O@PDA-C-20: 151 Ω, (Co,Fe)O@PDA-C-100: 150 Ω, (Co,Fe)O@PDA-C-200: 100 Ω, (Co,Fe)O: 217 Ω, and bare (Co,Fe)O: 133 Ω) was noticed for all composites. This reduction was attributed to the formation of the amorphous-like ultrafine (Co,Fe)O crystals within the structure during initial cycle (Fig. 6(b)) [41,56–58]. Following the 300th cycle (Fig. 6(c)), hollow (Co,Fe)O@PDA-C-100 porous nanocages exhibited the lowest R_{ct} value of 48 Ω compared to the (Co,Fe)O@PDA-C-20 (56 Ω), (Co,Fe)O@PDA-C-200 (54 Ω), (Co,Fe)O (64 Ω) and bare (Co,Fe)O nanocrystals (83 Ω). This observation points toward faster redox kinetics and advanced integrity of electrode specifically in (Co,Fe)O@PDA-C-100 porous nanocages. Moreover, the ionic diffusivity is an important factor for analyzing redox kinetics, the GITT measurements were

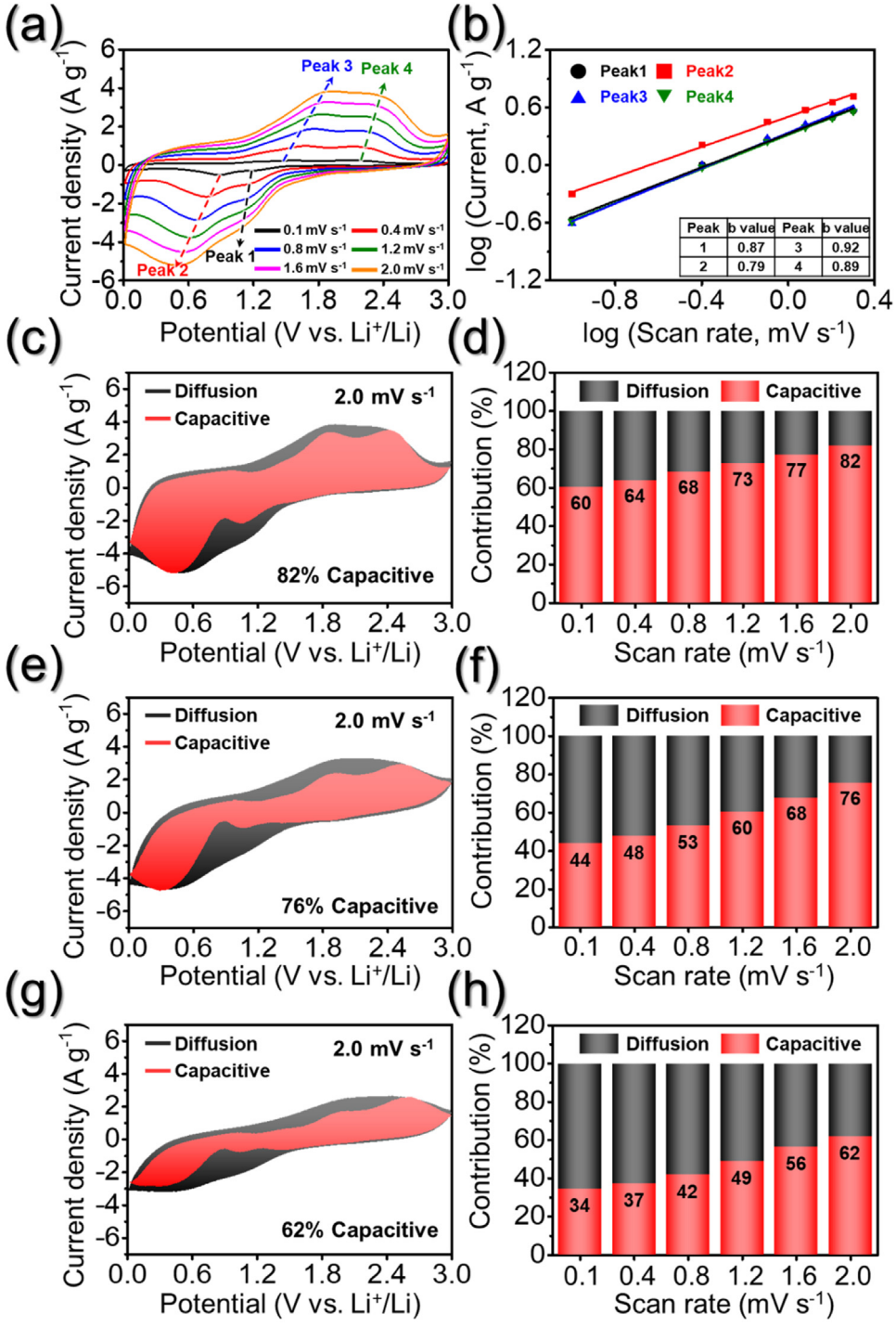

Fig. 5. Electrochemical reaction dynamics analysis of (a–d) the (Co,Fe)O@PDA-C-100, (e, f) (Co,Fe)O porous nanocages, and (g, h) bare (Co,Fe)O nanocrystals for Li-ion storage: (a) CV curves obtained at various scan rates, (b) current response (i) versus scan rate (n) at each redox peak, (c, e, g) CV curves with the capacitive fraction shown by the red region at a scan rate of 2.0 mV s^{-1}, and (d, f, h) bar charts showing the percentage of the capacitive contribution at different scan rates.

conducted to calculate the Li-ion diffusion coefficients D_{Li^+} values for (Co,Fe)O@PDA-C-100, (Co,Fe)O porous nanocages, and bare (Co,Fe)O nanocrystals. The GITT curves for three anodes shown in Figs. 6(d) and S19 were used to measure the variables required for the calculation, and the values were measured using the following equation [59]:

$$D_{Li^+} = \frac{4}{\pi\tau}\left(\frac{m_b V_M}{M_b S}\right)^2\left(\frac{\Delta E_s}{\Delta E_\tau}\right)^2\left(\tau \ll \frac{L^2}{D}\right) \quad (8)$$

where τ is the current pulse time (1200 s), m_b is the mass of active material (0.00182 g), V_M is the molar volume of the active material (42.03 cm^3 mol^{-1}), M_b is the molecular weight of active material (237.36 g mol^{-1}), S is the geometric area of the electrode (1.5386 cm^2), and ΔE_s is the potential change after every equilibrium process. The determination of ΔE_s and ΔE_τ values is presented in Fig. S20. As a result, the D_{Li^+} value for (Co,Fe)O@PDA-C-100 porous nanocages was calculated approximately 2.3 × 10^{-10} cm^2 s^{-1}, which is the highest compared to the (Co,Fe)O porous nanocages (9.0 × 10^{-11} cm^2 s^{-1}) and bare (Co,Fe)O nanocrystals

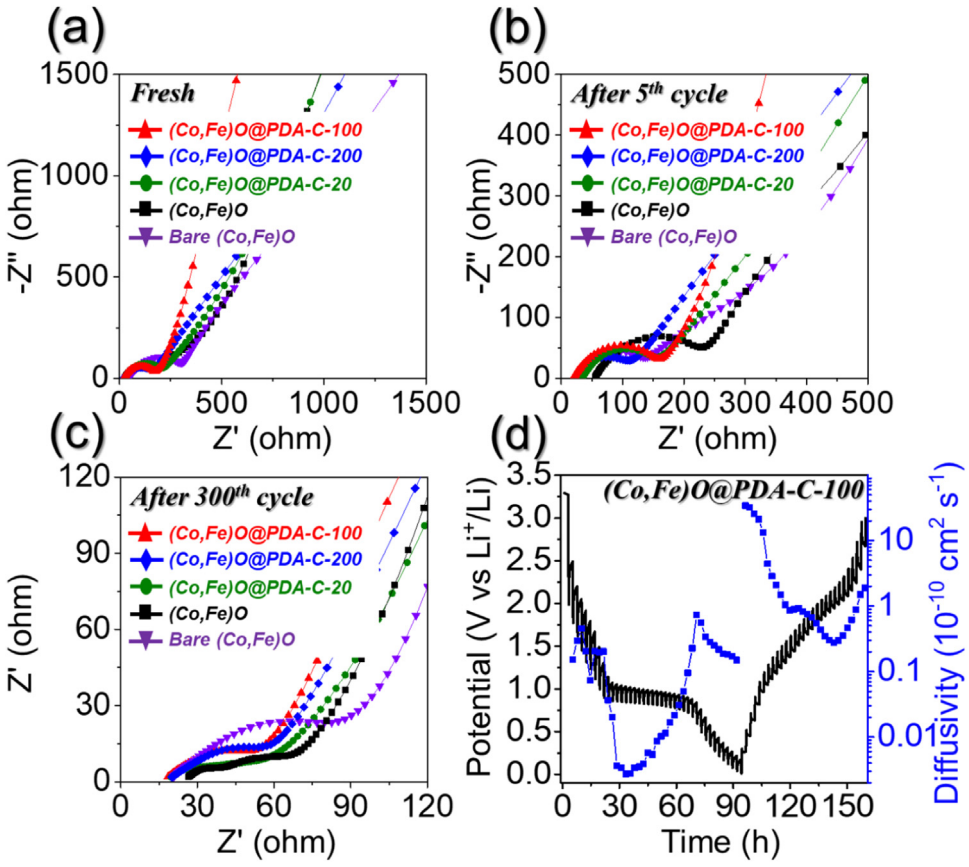

Fig. 6. (a–c) Nyquist impedance plots of assembled cells employed with different anodes during cycling at 0.5 A g^{-1} and (d) GITT curves of (Co,Fe)O@PDA-C-100 porous nanocages: (a) before cycling, (b) after 5th cycle, (c) after 300th cycle, (d) Li-ion diffusion coefficient (D_{Li^+}) measurement using GITT curve during discharge/charge process.

(6.1×10^{-11} cm^2 s^{-1}), as shown in Table S4. The higher D_{Li^+} value recorded for (Co,Fe)O@PDA-C-100 porous nanocages is attributed to the hollow structure composed of small-sized nanoparticles and mesopores derived form CoFe-PBA template, which facilitates better diffusion of charged species. The tiny size of nanocrystals (approximately 7 nm) reduced the diffusion length of Li-ion into the crystal structure, as well as the distribution of mesopores and hollow particles in the nanocage facilitated efficient electrolyte permeation into the nanostructures. Consequently, the D_{Li^+} value for (Co,Fe)O@PDA-C-100 anodes surpassed those of the (Co,Fe)O porous nanocages and bare (Co,Fe)O anodes, signifying remarkably rapid Li-ion diffusion and thus enhanced kinetics of redox reactions during the discharge/charge cycles. This result matched well with the rate performance shown in Fig. 4(e). Moreover, this higher diffusion value for (Co,Fe)O@PDA-C-100 porous nanocages corroborated the structural robustness of prepared composite, enabling it to endure longer cycling durations while upholding the mechanical integrity of the electrode.

The post-cycled SEM images (Fig. S21(a–e)) of electrode materials were recorded after 300 cycles at 0.5 A g^{-1} to elucidate the variance in R_{ct} among the electrodes. Comparatively, the R_{ct} of (Co,Fe)O@PDA-C-20, (Co,Fe)O@PDA-C-100, (Co,Fe)O@PDA-C-200, and (Co,Fe)O nanocages were significantly lower than that of the bare (Co,Fe)O nanocrystals. This difference is attributed to the structural robustness through the porous structure constructed by well-defined (Co,Fe)O particles, providing significant advantages in long-term cycling performance, as shown in the SEM images displayed in Fig. S21(a–d). Conversely, the bare (Co,Fe)O nanocrystals proved incapable of enduring the stress incurred during cycling, resulting in the formation of bulky agglomerates. This transformation led to the highest R_{ct} after 300 cycles among the five electrode materials, as illustrated in Fig. S21(e).

Furthermore, full-cells comprising the (Co,Fe)O@PDA-C-100 anode paired with $Li(Ni_{0.8}Co_{0.1}Mn_{0.1})O_2$ (NCM811) cathode were prepared to investigate the practical application potential of the prepared anode, and electrochemical analysis results of the full-cells were shown in Fig. 7. Prior to full-cell test, the physical and electrochemical properties of the NCM811 were examined as shown in Fig. S22, followed by a detailed discussion. The full-cells were cycled in the voltage range of 0.5–4.2 V, and the active material loading masses of the anode and cathode were fixed at approximately 2.05 and 8.6 mg cm^{-2} (N/P ratio ≈ 1.2), respectively, to satisfy the condition of practical application. Fig. 7(a) illustrates the schematic of the full-cell comprising the NCM811//(Co,Fe)O@PDA-C-100 pair. The full-cell comprising the NCM811//(Co,Fe)O@PDA-C-100 pair displayed 4.2 V after fully charging at 0.1 C, and powered a light-emitting diode (5 V, 10 mW), emphasizing the large-scale energy-storage capability of the full-cell (Fig. 7(b)). The initial voltage profiles of full cell at 0.1 and 0.5 C exhibited charge/discharge capacities of 204/182 and 149/151 mA h g^{-1}, respectively (Fig. 7(c)). Moreover, when cycled at 0.5 C, the cell displayed discharge capacities of 165 mA h g^{-1} after 50 cycles and a high CE of 99.93%, suggesting the practical viability of the prepared nanostructure as an anode (Fig. 7(d)). The rate performance of the full-cell was also noteworthy, with considerable discharge capacities of 183, 174, 164, 149, 128, 103, 87, 66, and 45 mA h g^{-1} at 0.1, 0.3, 0.5, 0.7, 1.0, 1.5, 2.0, 3.0, and 5.0 C, respectively (Fig. 7(e)). Overall, the full-cell results indicated that the prepared anode nanostructure

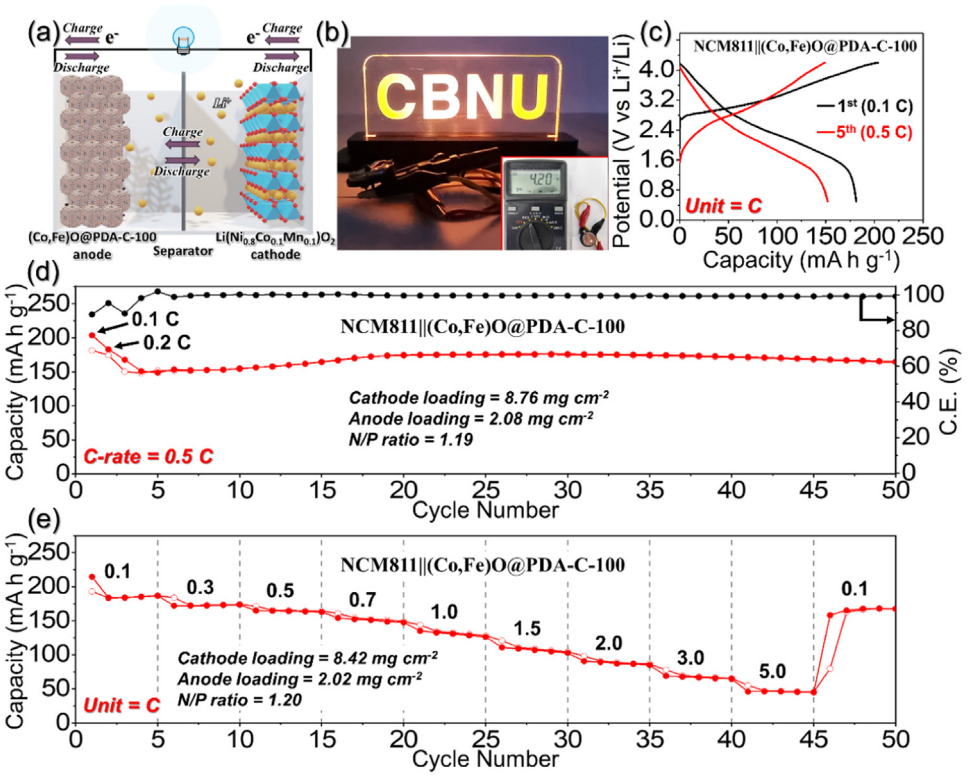

Fig. 7. (a) Schematic diagram of full-cell consisting of $Li(Ni_{0.8}Co_{0.1}Mn_{0.1})O_2$ (NCM811) cathode and (Co,Fe)O@PDA-C-100 anode, (b) digital image of a light-emitting diode (5 V, 10 mW) powered by one cell utilized after fully charging at 0.1 C (1.0 C = 180 mA g^{-1}), (c) initial galvanostatic charge/discharge voltage profiles at current densities of 0.1 and 0.5 C, (d) cycling performance at 0.5 C, and (e) rate performance.

has practical application potential to be coupled with NCM811 cathode.

4. Conclusion

This study presents for the first time an innovative and facile synthesis strategy fabricating porous nanocages comprising hollow (Co,Fe)O nanoparticles through a straightforward process involving co-precipitation and subsequent Kirkendall diffusion process by optimization of solution-based PDA-derived carbon coating content. The porous structure originated from the CoFe-PBA template provides ample space to manage substantial volume stresses and enables effective electrolyte penetration, ensuring rapid diffusion of charge species. In addition, the hollow nanoparticles through the controlled oxidation rate of (Co,Fe) nanocrystals regulated by optimized PDA content shorten the diffusion pathways for charge species, facilitating rapid charge transfer and supporting efficient redox reactions kinetics. Benefited from the structural advantages, when employed as anode for LIBs, the hollow (Co,Fe)O@PDA-C-100 porous nanocages exhibit both structural robustness and high-rate capabilities. Particularly noteworthy is their cycling stability, demonstrating the capacity retention of 97.2% after the 300th cycle at a current density of 1.0 A g^{-1}, and high discharge capacity of 284 mA h g^{-1} at a high current density of 10 A g^{-1}, showcasing effectiveness of this approach in attaining great electrochemical performance at high charging rates. Furthermore, the practical application potential of the prepared hollow (Co,Fe)O@PDA-C-100 anode was demonstrated by full-cell test paired with $Li(Ni_{0.8}Co_{0.1}Mn_{0.1})O_2$ cathode under the condition of practical application (the active material loading masses of the anode and cathode were fixed at approximately 2.05 and 8.6 mg cm^{-2}). Thus, the structural enhancements demonstrated in this research hold promise for enabling highly conductive and porous hollow heterostructures, crucial for ensuring stable cycle life in diverse energy-related applications.

Declaration of competing interest

The authors declare that they have no known competing financial interests or personal relationships that could have appeared to influence the work reported in this paper.

CRediT authorship contribution statement

Jae Seob Lee: Writing – original draft, Visualization, Project administration, Investigation, Data curation, Conceptualization. **Kun Woo Baek:** Writing – original draft, Visualization, Validation, Methodology, Data curation, Conceptualization. **Narasimharao Kitchamsetti:** Writing – review & editing, Writing – original draft, Data curation. **Hyun Woo Kim:** Data curation, Resources. **Jung Sang Cho:** Writing – review & editing, Visualization, Supervision, Investigation, Funding acquisition, Conceptualization.

Acknowledgments

This work was supported by the National Research Foundation of Korea (NRF) and the Commercialization Promotion Agency for R&D Outcomes (COMPA) funded by the Ministry of Science and ICT (Nos. RS-2023-00217581 and RS-2023-00304768). Following are results of a study on the "Leaders in INdustry-university Cooperation 3.0" Project, supported by the Ministry of Education and National Research Foundation of Korea.

Supplementary materials

Supplementary material associated with this article can be found, in the online version, at doi:10.1016/j.jmst.2024.10.026.

References

[1] N. Kitchamsetti, J.S. Cho, J. Energy Storage 80 (2024) 110293.
[2] N. Kitchamsetti, J. Energy Storage 73 (2023) 108958.
[3] X.K. Wang, L. Hao, R.X. Du, H. Wang, J.X. Dong, Y.F. Zhang, J. Colloid Interface Sci. 653 (2024) 730–740.
[4] Z. Gao, C. Zhao, K. Zhou, J. Wu, Y. Tian, X. Deng, L. Zhang, K. Lin, F. Kang, L. Peng, M. Wagemaker, B. Li, Nat. Commun. 15 (2024) 1503.
[5] N. Kitchamsetti, D. Kim, Electrochim. Acta 441 (2023) 141824.
[6] F. Bu, M.M. Zagho, Y. Ibrahim, B. Ma, A. Elzatahry, D. Zhao, Nano Today 30 (2020) 100803.
[7] N. Kitchamsetti, D. Kim, J. Alloy. Compd. 959 (2023) 170483.
[8] J.S. Lee, N. Kitchamsetti, J.S. Cho, Chem. Eng. J. 487 (2024) 150465.
[9] S.-H. Yu, S.H. Lee, D.J. Lee, Y.-E. Sung, T. Hyeon, Small 12 (2016) 2146–2172.
[10] R.A. Ntiamoah, H. Kim, ChemSusChem 17 (2024) e202400085.
[11] J. Wang, X.K. Fan, X. Han, K. Lv, Y.J. Zhao, Z.W. Zhao, D.Y. Zhao, Adv. Mater. 36 (2024) 2312374.
[12] Y.W. Niu, X.Y. Zhang, Y.X. Kang, P.L. Sun, H.Q. Liu, Z.B. Xiao, D. Zhao, Mater. Today Commun. 39 (2024) 108660.
[13] P. Tang, J.W. Du, M. Li, X.Y. Zhao, H.Q. Ren, X.Y. Zhang, G.H. Wu, X.W. Wang, ACS Appl. Nano Mater. 7 (2024) 10325–10337.
[14] H.S. Kang, P. Santhoshkumar, J.W. Park, G.S. Sim, M. Nanthagopal, C.W. Lee, Korean J. Chem. Eng. 37 (2020) 1331–1339.
[15] S.Q. Li, Y. Ye, X. Liu, X.R. Yang, S. Fang, N.G. Zhou, Chem. A Eur. J. 30 (2024) e202302768.
[16] C. Yuan, H.B. Wu, Y. Xie, X.W. (David) Lou, Angew. Chem. Int. Ed. 53 (2014) 1488–1504.
[17] M.V. Reddy, G.V. Subba Rao, B.V.R. Chowdari, Chem. Rev. 113 (2013) 5364–5457.
[18] M. Yang, C.H. Zhang, N.W. Li, D.Y. Luan, L. Yu, X.W. Lou, Adv. Sci. 9 (2022) 2105135.
[19] Y.P. Chen, Y. Yao, W.T. Zhao, L.F. Wang, H.T. Li, J.W. Zhang, B.J. Wang, Y. Jia, R.G. Zhang, Y. Yu, J. Liu, Nat. Commun. 14 (2023) 7487.
[20] G. Song, Y. Shi, S. Jiang, H. Pang, Adv. Funct. Mater. 33 (2023) 2303121.
[21] G. Zhu, D. Luo, X. Chen, J. Yang, H. Zhang, ACS Nano 17 (2023) 20850–20874.
[22] J.M.J. Santillán, D.M. Arboleda, D.F. Coral, M.B.F. Raap, D. Muraca, D.C. Schinca, L.B. Scaffardi, ChemPhysChem 18 (2017) 1192–1209.
[23] A. Diallo, A.C. Beye, T.B. Doyle, E. Park, M. Maaza, Green Chem. Lett. Rev. 8 (2015) 30–36.
[24] J.S. Lee, R. Saroha, J.S. Cho, Nano-Micro Lett. 14 (2022) 113.
[25] Z. Yan, Y. Kang, D. Li, Y.C. Liu, Korean J. Chem. Eng. 37 (2020) 623–632.
[26] N. Kitchamsetti, R.J. Choudhary, D.M. Phase, R.S. Devan, RSC Adv. 10 (2020) 23446–23456.
[27] J.H. Park, S. Jo, N. Kitchamsetti, S. Zaman, D.W. Kim, J. Alloy. Compd. 926 (2022) 166815.
[28] S. Jo, N. Kitchamsetti, H.W. Cho, D.W. Kim, Polymers 15 (2023) 454.
[29] S.K. Park, Y.C. Kang, ACS Appl. Mater. Interfaces 10 (2018) 17203–17213.
[30] D. Li, J.S. Zhou, X.H. Chen, H.H. Song, ACS Appl. Mater. Interfaces 10 (2018) 22841–22850.
[31] Y. Chen, J. Shao, X.Y. Lin, Y.Y. Gu, R. Holze, Y.X. Yun, Q.T. Qu, H.H. Zheng, ChemElectroChem 6 (2019) 1393–1399.
[32] R. Xu, Y. Yao, H.Y. Wang, Y.F. Yuan, J.W. Wang, H. Yang, Y. Jiang, P.C. Shi, X.J. Wu, Z.Q. Peng, Z.S. Wu, J. Lu, Y. Yu, Adv. Mater. 32 (2020) 2003879.
[33] B. He, G.Y. Li, J.J. Li, J. Wang, H. Tong, Y. Fan, W.L. Wang, S.H. Sun, F. Dang, Adv. Energy Mater. 11 (2021) 2003263.
[34] Y.F. Xu, H.D. Zhang, D. Gong, Y.X. Chen, S.W. Xu, P. Qiu, J. Mater. Sci. 57 (2022) 19716–19729.
[35] X. Jiang, G.F. Shi, G.Y. Wang, P. Mishra, J.W. Du, Y. Zhang, Ionics 26 (2020) 4039–4051.
[36] J.S. Lee, M.S. Jo, R. Saroha, D.S. Jung, Y.H. Seon, J.S. Lee, Y.C. Kang, D.W. Kang, J.S. Cho, Small 16 (2020) 2002213.
[37] J.S. Lee, R. Saroha, S.H. Oh, D.H. Shin, S.M. Jeong, J.K. Kim, J.S. Cho, Small Methods 5 (2021) 2100195.
[38] L.S. Xia, Z.D. Yang, B. Tang, F. Li, J.P. Wei, Z. Zhou, Small 17 (2021) 2006016.
[39] Z.G. Wu, Y.J. Zhong, J.T. Li, K. Wang, X.D. Guo, L. Huang, B.H. Zhong, S.G. Sun, RSC Adv. 6 (2016) 54404–54409.
[40] F. Li, G.H. Zhai, H.J. Ren, G. Wang, H. Wang, Ionics 24 (2018) 111–120.
[41] J.S. Cho, Y.J. Hong, Y.C. Kang, ACS Nano 9 (2015) 4026–4035.
[42] J. Luo, J. Liu, Z. Zeng, C.F. Ng, L. Ma, H. Zhang, J. Lin, Z. Shen, H.J. Fan, Nano Lett. 13 (2013) 6136–6143.
[43] J. Sun, H. Wang, Y. Li, M. Zhao, J. Porous Mater. 28 (3) (2021) 889–894.
[44] P. Kulkarni, R.G. Balkrishna, D. Ghosh, R.S. Rawat, R. Medwal, B.V.R. Chowdari, Z. Karim, M.V. Reddy, Mater. Chem. Phys. 257 (2021) 123747.
[45] Y. Wu, Y. Wei, J. Wang, K. Jiang, S. Fan, Nano Lett. 13 (2013) 818–823.
[46] S. Laruelle, S. Grugeon, P. Poizot, M. Dollé, L. Dupont, J.-M. Tarascon, J. Electrochem. Soc. 149 (2002) A627–A634.
[47] Z. Wang, D. Luan, S. Madhavi, Y. Hu, X.W. Lou, Energy Environ. Sci. 5 (2012) 5252–5256.
[48] Y. Yu, C.-H. Chen, J.-L. Shui, S. Xie, Angew. Chem. Int. Ed. 44 (2005) 7085–7089.
[49] S.H. Choi, Y.C. Kang, Carbon 79 (2014) 58–66.
[50] X. Huang, J. Chen, Z. Lu, H. Yu, Q. Yan, H.H. Hng, Sci. Rep. 3 (2013) 2317.
[51] Y. Ma, P. Liu, Q. Xie, C. Zhang, L. Wang, D.-L. Peng, Mater. Today Energy 16 (2020) 100383.
[52] Q. Wang, D. Chen, J. Chen, C. Lai, L. Li, C. Wang, Mater. Lett. 141 (2024) 319–322.
[53] J.S. Lee, J.-S. Park, K.W. Baek, R. Saroha, S.H. Yang, Y.C. Kang, J.S. Cho, Chem. Eng. J. 456 (2023) 141118.
[54] P. Ge, L. Zhang, Y. Yang, W. Sun, Y. Hu, X. Ji, Adv. Mater. Interfaces 7 (2020) 1901651.
[55] N.Y.W. Zaw, S. Jo, J.H. Park, N. Kitchamsetti, N. Jayababu, D.W. Kim, Appl. Clay Sci. 225 (2022) 106539.
[56] M.J. Jin, G.W. Sun, J.S. Yuan, Y.T. Wang, J.Y. Zhou, J. Li, X. Ni, X.J. Pan, E. Xie, J. Alloy. Compd. 922 (2022) 166231.
[57] Q.D. Hou, Q. Man, P.F. Liu, R.C. Jin, Y.M. Cui, G.H. Li, S.M. Gao, Electrochim. Acta 296 (2019) 438–449.
[58] J.S. Lee, R. Saroha, J.H. Oh, C. Cho, B. Jin, D.-W. Kang, J.S. Cho, J. Ind. Eng. Chem. 114 (2022) 276–287.
[59] X. Liu, R. Wang, S. Liu, J. Pu, H. Xie, M. Wu, D. Liu, Y. Li, J. Liu, Adv. Energy Mater. 13 (2023) 2302987.